LUNFD6/(NFFL-7215)2003

The Unintegrated Gluon Density In The Photon And Heavy Quark Production

Diploma Thesis
by

Magnus Hansson

LUND
UNIVERSITY

DEPARTMENT OF HIGH ENERGY PHYSICS
LUND, 2003

Abstract

The production cross section of heavy quarks in real and virtual photon-photon collisions has been studied. The unintegrated gluon density in the photon was obtained using the CCFM evolution equation for the first time. The gluon density was implemented in the Monte Carlo generator CASCADE, and cross sections for heavy quark production in e^+e^- collisions were calculated and compared to LEP data. Also, predictions for heavy quark cross sections in e^+e^- and $\gamma\gamma$ collisions at TESLA energies are given.

Contents

Chapter 1

Introduction

By convention there is color,
By convention sweetness,
By convention bitterness,
But in reality there are atoms and space.

Around 400 B.C. the greek philosopher Democritus proposed that matter cannot be divided in arbitrary small pieces, but consists of some fundamental particles which he called atoms. This was in great conflict with the then dominating belief that matter was continous and consisted of the four elements earth, water, fire and air. Indeed, the theory with the four elements was the dominating one for over 2000 years, but had to be abandoned during the 18th century, when, among other discoveries, air was separated into its constituents. This resulted in an atomic theory, proposed in the beginning of the 19th century, where the atom was a homogenious ball. This model was drastically changed in the beginning of the 20th century, when the atom was found to consist of electrons and a small, but massive core, indicating that the atoms were not the most fundamental particles. Later, the core was found to consist of protons and neutrons, which in turn consists of quarks. The electrons and the quarks (and some other particles) are today believed to be fundamental, that is, they have no internal structure. It is the properties and interactions of these that are studied in particle physics. Due to the development of quantum mechanics and the construction of particle accelerators, the past century offered many important discoveries, providing a more fundamental understanding of the constituents of matter and its interactions, which resulted in the Standard Model.

1.1 The Standard Model

In particle physics today, the theory describing the building bocks of nature and their interactions is called the Standard Model (SM). In this theory, everything consists of quarks and leptons (of which the electron is one), and their anti-particles. These particles are divided into three families, see Figure 1.1. Only the first family is stable, and hence all particles we see in nature consist of u and d quarks and electrons. All other particles can only be seen in particle accelerators or in cosmic radiation collisions. Particles consisting

of quarks are called hadrons. There are two types of hadrons: baryons, which consist of three quarks (e.g. protons (uud) and neutrons (udd)), and mesons, which consist of one quark and one anti-quark. All mesons are unstable, even if they consist of quarks from the first family, since in these cases the quark and anti-quark annihilate after some time and decay into leptons and photons.

$$\begin{array}{cccc} -1 & \begin{pmatrix} e^- \\ \nu_e \end{pmatrix} & \begin{pmatrix} \mu^- \\ \nu_\mu \end{pmatrix} & \begin{pmatrix} \tau^- \\ \nu_\tau \end{pmatrix} \\ 0 & & & \end{array}$$

$$\begin{array}{cccc} +2/3 & \begin{pmatrix} u \\ d \end{pmatrix} & \begin{pmatrix} c \\ s \end{pmatrix} & \begin{pmatrix} t \\ b \end{pmatrix} \\ -1/3 & & & \end{array}$$

Figure 1.1: *The three particle families in the Standard Model. The leptons are the electron, muon and tau particles with corresponding neutrinos. The quarks are called up, down, charm, strange, top and bottom (or beauty). Also shown are the electromagnetic charges in units of e.*

The interaction between these particles is described by four forces, which are mediated by the exchange of virtual particles called gauge bosons. A particle is called virtual when energy is not conserved in its creation. This is possible due to the Heisenberg uncertainty principle

$$\Delta E \cdot \Delta t \sim \hbar$$

where ΔE is the uncertainty in energy, Δt is a time interval and $\hbar = 1.05 \cdot 10^{-34}$ Js is the Planck constant. This means that a particle with energy ΔE (including mass, since $E = mc^2$ for a particle at rest) can be created out of the vacuum, but it can only exist during a time interval $\Delta t \sim \frac{\hbar}{\Delta E}$. Thus, the higher the energy of the particle the shorter the lifetime, and the shorter the lifetime the shorter the particle can travel during a time interval Δt. This is the basic idea for understanding the range of the forces.

The electromagnetic (EM) force acts between all electrically charged particles and composite particles with a net EM charge, including all quarks, the charged leptons, protons etc., and it is mediated by photons. Due to the fact that photons are massless and do not carry EM charge themselves, they can not interact mutually, and therefore the EM force has an infinite range. The theory describing the EM force is called Quantum Electro Dynamics (QED).

The weak force is mediated by the W^+, W^- and Z^0 particles, and affects all particles with so called weak charge. These include all quarks and leptons. The weak force is responsible for the decay of the heavier quarks and leptons, and thus also for β-decay, $n \rightarrow p + e^- + \bar{\nu}$, which involves the transition $d \rightarrow u$. The W^+, W^- and Z^0 particles are very heavy (80 GeV and 91 GeV respectivly, which can be compared to the proton mass $m_P = 0.9$ GeV) and hence the range of the weak force is very small, about 10^{-18} m, or one thousand times smaller than the size of a proton.

The strong force, or the color force, is responsible for binding the quarks inside the hadrons, and binding hadrons to nuclei. This force is mediated by 8 gluons, and interacts

between all particles carrying color charge, i.e. quarks and the gluons themselves. Quarks can have either red, blue or green color charge (anti-quarks have anti-red, anti-blue or anti-green charge) and gluons carry the charge of one color and one anti-color. These color charges have nothing to do with the colors we see around us. The selfcoupling of the gluons has two very important consequences. One is that, although the gluons are massless, the strong force has a very short range ($\sim 10^{-15}$ m, which is the size of a proton). The other is that the strong force is weak at small distances, so called asymptotic freedom, and becomes stronger as the distance increase, which leads to confinement of the quarks. As a consequence, the quarks inside hadrons seem to be moving freely, but when one tries to knock out a quark, the field strenght between the quarks becomes stronger. When the energy in the field exceeds the mass of the lightest hadrons, the field may break up and new, colorless, hadrons are created. So far, free quarks, or indeed any colored object, has never been directly observed. The theory describing the strong force is called Quantum Chromo Dynamics (QCD).

Gravity is the weakest force and interacts between all massive particles. There are attempts to include gravity in a quantum theory where gravitons act as mediators. Due to the weakness of the force and the small masses of the particles involved, gravity is normally neglected in the discussion of particle physics processes.

Force	*Mediators*	*Relative strength*	*Range (m)*
The strong force	Gluons	1	10^{-15}
The electromagnetic force	Photons	10^{-2}	∞
The weak force	W^+, W^- and Z^0	10^{-5}	10^{-18}
The gravitational force	Gravitons	10^{-39}	∞

Table 1.1: *Comparison of the four forces in Nature.*

The SM is a very succsessful theory, but it is nevertheless incomplete. For example, there are many (~ 20) parameters, including all the particle masses and couplings, which are not fixed by theory, but must rather be measured. Another problem is the arbitraryness of the theory, that is, the theory has been adjusted to Nature by hand without any other fundamental reason. This includes the number of families, the three groups SU(3), SU(2) and U(1) which gives the interactions, and that fermions are treated differently depending on the direction of their spin and momentum. A complete theory should of course also include gravitation and provide answers to the problems with dark matter and the cosmological constant. Some of the new theories and their signatures in $\gamma\gamma$ collisions will be briefly discussed in Chapter 2.

Chapter 2

Accelerators and detectors

As the particles we want to probe become smaller, and the new particles we want to create become heavier, higher energies, and hence better accelerators, are needed. Accelerators demand a lot of knowledge, manpower and money and are therefore built and maintained by large international collaborations, and concentrated at a few facilities around the world.

2.1 Accelerator parameters

From the physics point of view, there are three main properties that characterize an accelerator. The first property concerns **the kind of particles to be accelerated**. Any charged, long-lived, particles can be used, like electrons, positrons, protons, anti-protons and ions. Examples are LEP (e^+e^-), the TEVATRON ($p\bar{p}$) and HERA ($e^{+/-}p$). The second property is the **center of mass (c.m.) energy** of the collision, denoted $\sqrt{s}$. The c.m. energy is the energy that can be used for the production of particles, and is determined by the final energy and the mass of the accelerated particles. The most efficient use of the energy is achieved when two pointlike particles with the same mass, like electrons or positrons, collide head on with equal but opposite momenta. Then all of the energy is useful energy, i.e. $\sqrt{s} = 2E$, where E is the energy of the particles. When the particles do not have equal but opposite momenta, like in $e^{+/-}p$ or fixed target collisions, some of the energy must be used for the motion of the center of mass, making the useful energy smaller than the sum of the energies of the colliding particles. Also, when using composite particles like protons and anti-protons, the energy is shared by the constituents, with the consequence that all the c.m. energy is not used in the collisions, and that the colliding constituents most often have unequal momenta. However, in such collisions, the energy of the particles is often much higher, resulting in a higher useful energy compared to e^+e^- collisions. This is due to the fact that usually circular colliders are used, and that charged particles emit synchrotron radiation when accelerated in circles according to

$$\Delta E \propto \left(\frac{E}{m}\right)^4,$$

where ΔE is the energy loss, and E and m is the energy and mass of the particle, respectively. (The energy loss also depends on the charge and speed of the particle, and

on the radius of curvature.) This means that lighter particles emit more synchrotron radiation than heavier ones with the same energy, and that the radiation increases rapidly with the energy. The energy loss must be compensated for and additional energy must be transferred in order to continue the acceleration. Therefore LEP is believed to be the last circular collider which uses electrons and positrons. For heavier particles, such as protons, the problem is not that severe due to the much higher mass, and very high energies can be achieved in circular colliders. It is estimated that for e^+e^- accelerators with $\sqrt{s} > 200$ GeV, linear accelerators will be the only reasonable choice. This, however, requires the development of a new accelerator technology. The third property is the **luminosity**, $\mathcal{L}$. This is, like the final energy, a machine property, and describes how efficiently the particle bunches are directed in the collisions. The luminosity can be written as $\mathcal{L} = fnk^2/A$, were f is the frequency with which the bunches collide, n is the number of bunches, k is the number of particles per bunch and A is the cross sectional area of the beam. The luminosity is the proportionality factor in the relation between the number of events, N, and the cross section (which is a measure of the probability of a certain process to occur), σ,

$$N = \int \mathcal{L} dt \sigma.$$

2.2 TESLA

TESLA (TeV Energy Superconducting Linear Accelerator) is a proposed e^+e^--collider currently being planned and developed at DESY, Hamburg. The accelerator, consisting of two 15-kilometer sections with about 20 000 accelerating structures, would have one end at the DESY site and the other end 33 km north-northwest of DESY, with a collision zone in between. At a first stage, a c.m. energy of $\sqrt{s} = 500$ GeV could be achieved, and by increasing the acceleration field further $\sqrt{s} = 800$ GeV will be possible. This offers a unique possibility to make precision measurements of fundamental properties in particle physics, and also to search for new physics. The precise task of TESLA depends on the results of the experiments at the TEVATRON and the LHC, but it will undoubtebly concern the Higgs boson and the search for new physics. Some possible scenarios are:

- New physics is discovered at the TEVATRON and/or the LHC. TESLA would then study these particles and/or interactions in detail in order to reveal the underlying theories.
- The Higgs boson is found at the TEVATRON and/or the LHC, but no new physics is found. The task of TESLA would then be to do precision measurements of the Higgs boson, the electroweak gauge bosons and the top quark to search for deviations from SM predictions, which would be a sign of new physics.
- The electroweak symmetry breaking (the Higgs mechanism in the SM) is found to be dynamical. This would indicate that new particles (techniquarks) and a new strong force (technicolor) could be found at the TeV scale. Indications of this could be found by studying the interactions of the W bosons and the t quarks.
- If nothing is found at the TEVATRON or the LHC, TESLA would of course continue the search for the Higgs boson and new physics.

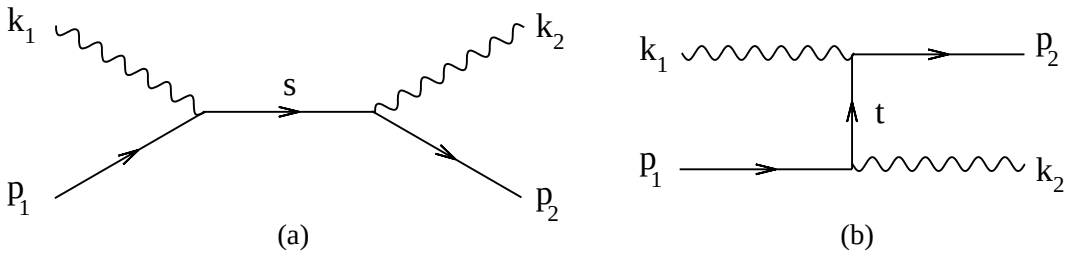

Figure 2.1: *The Feynman diagrams for Compton scattering: the s-channel (a) and the t-channel (b).*

2.3 The photon-photon-collider at TESLA

As an extension of TESLA, a $\gamma\gamma$ -collider [1] could be implemented, which, for the first time, would give the possibility to collide photons with photons and photons with electrons, where all the photons are real. This would require an additional collision zone and high energy lasers.

2.3.1 The interaction region

When a photon (k_1) collides with an electron (p_1), the photon may be Compton scattered via one of the two processes shown in Figure 2.1. At high energies, the s-channel process (a) can be neglected since the cross section is proportional to $\frac{1}{s^2} = \frac{1}{(p_1+k_1)^2}$. The cross section for the t-channel process is proportional to $\frac{1}{t^2}$, where $t = p_1 - k_2$. This means that the cross section is large when $p_1 \approx k_2$, i.e. when the photon is emitted in the direction of the incoming electron with an energy similar to the energy of the incoming electron. This is the basic principle of producing high energy photons at the $\gamma\gamma$ -collider, where the incoming electron is accelerated in TESLA and the incoming low energy photons are produced by a laser.

The interaction region is shown schematically in Figure 2.2. In order to avoid background from the disrupted beams, a crab crossing scheme is used (b), where the beams collide under a small angle α_c. In the present design, $\alpha_c = 34$ mrad. The e^- bunches would be directed to the collision zone and collide with laser photons at a distance b from the interaction point (IP). The exact distance between this conversion point (CP) and the IP depends on the energy of the electron beam, the electron bunch size and the size of the conversion region, but it is of the order of a few mm. The photons, which initially have an energy $\omega_0 = 1.17$ eV ($\lambda = 1.06$ μm), will after Compton scattering have a maximum energy of about 80% of the electron beam energy, i.e. $\omega_{max} \approx 200$ GeV for an electron energy of $E = 250$ GeV. By having very small electron bunch sizes and by using polarised electron beams, this conversion can be made very efficiently. The photons will of course have a continous spectrum, but it will be peaked at ω_{max} if the electron and photon polarisations are tuned properly. After the conversion, the photons travel to the IP and collide with the photons from the other beam. Because of the small distance between the CP and the IP, it is not possible to remove the electron beam prior to the collision point by using magnets.

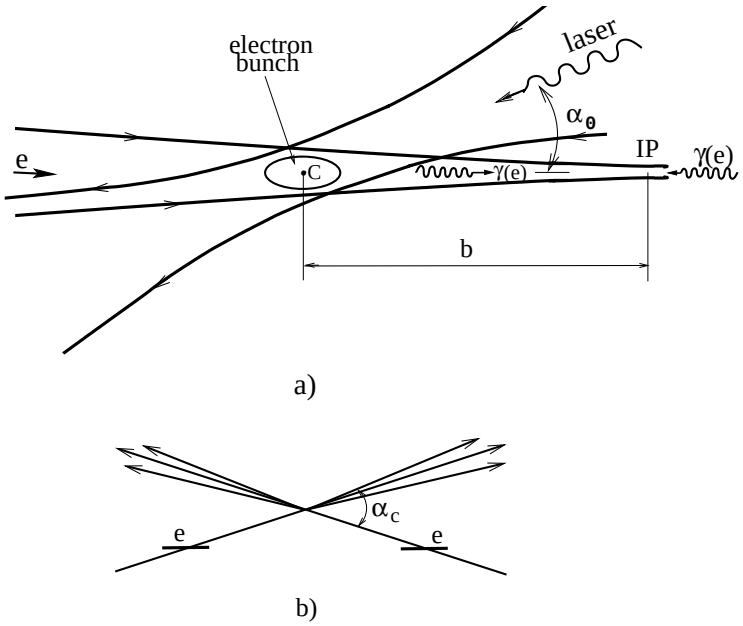

Figure 2.2: *The interaction region: the conversion and interaction point (a) and the crab crossing scheme (b).*

Hence, all particles will travel to the IP producing e^-e^- and γe collisions as well as $\gamma\gamma$ collisions.

2.3.2 Laser and optics

A powerful laser with high flash energies, high repetition rate and a pulse duration of the order of picoseconds is a key element for the photon collider. The technology for solid state lasers with the required flash energies and pulse duration already exists. However, to accomplish a high repetition rate, two optical schemes are considered: the optical storage ring and the optical cavity. Both are based on the principle of using one laser pulse for many $e \rightarrow \gamma$ conversions. This is possible because a laser flash with an energy of 5 J (and $\lambda \approx 1$ μm) contains about $2 \cdot 10^{19}$ photons, but only about 10^{10} photons are used per collision, since there are only $2 \cdot 10^{10}$ electrons per bunch. With this approach, the laser pulse can be built up during the time between bunch train collisions. The required repetition rate for the laser would be about 14 kHz, which is much less than the 3 MHz repetition rate for the electron bunches in the bunch trains. (The repetition rate for the bunch trains is 5 Hz.) Another possibility to get a high repetition rate is to use a Free Electron Laser (FEL), but this requires one additional accelerator of a few hundred meters.

The optical storage ring: The most promising scheme for the optical "trap" is shown in Figure 2.3. Here, the photons make several round trips and collide with the electron bunches two times per loop, with an interval of 337 ns (which is the interval between beam collisions at TESLA). The photons enter the optical storage ring through the Thin Film Polarisers (TFP) and the Pockel cell (P). The TFP is transparent to light polarised in one direction, and reflects light with the orthogonal polarisation. The polarisation can

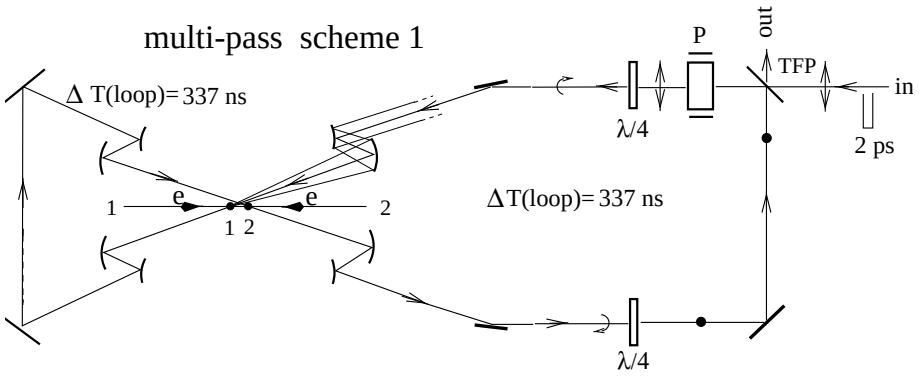

Figure 2.3: *The optical storage ring.*

be changed by 90° with the Pockel cell. The pulse then passes the 1/4 wavelenght plate ($\lambda/4$), giving a circular polarised beam. If linear polarisation is wanted in the collision, 1/2 wavelenght plates should be used. The polarised photon beam is then directed by mirrors to collide with electron beam 1, and, 337 ns later, with electron beam 2. The photon beam can then either be reflected by the TFP to make another round trip, or be removed from the system, depending on the polarisation of the beam. There are two main parameters that determine the number of loops: the attenuation of the pulse and non-linear effects (self focusing of the beam as a whole and self focusing and amplification of non-uniformities in the beam). In the scheme in Figure 2.3, the total loss/loop is about 5%, and 6 round trips (12 collisions) per pulse is estimated to be possible. It turns out that the non-linear effects can be made small by using appropriate Pockel cells. One can also avoid this problem by compressing and streching the laser pulse, but this results in large additional attenuation. The laser system required to produce the pulse trains for the storage ring is shown schematically in Figure 2.4. A low energy laser produces a 1 ms train with about 500 pulses (not shown in the figure). The train is split up in 8 subtrains, each with 62 pulses and a duration of 1 ms. These subtrains are distributed between eight amplifiers, where each pulse is amplified to 5 J, and is then recombined to form the final train.

The optical cavity: Another possible solution is the optical cavity, shown in Figure 2.5. The deformable mirrors M_1 and M_2 direct the low energy laser pulse train to the cavity and make sure that the incoming pulse and the pulse inside the cavity interfere constructively. Mirror M_3 should have a reflectivity of 99%, so 1% of the light is transferred to the CCD camera. The information from the CCD camera is used to adjust mirrors M_1 and M_2, but also M_4 and M_8 in order to maintain the phase of the laser wave. The mirrors M_4 to M_8 are optimized for maximum reflectivity. (Two mirrors, not shown in the figure, would be used to remove the photon beam.) In this way, the intensity of the laser pulse can be increased by a factor $Q \approx 50 - 100$, which is sufficient for the photon collider. Scattered electrons and synchrotron radiation will gradually damage the mirrors, resulting in a decrease of the Q-factor. This can be avoided by protecting the mirrors with thin glass plates. A possible laser for the optical cavity is a diode pumped solid state laser with ytterbium doped YAG, which can generate picosecond pulses with an average power up to 1 kW.

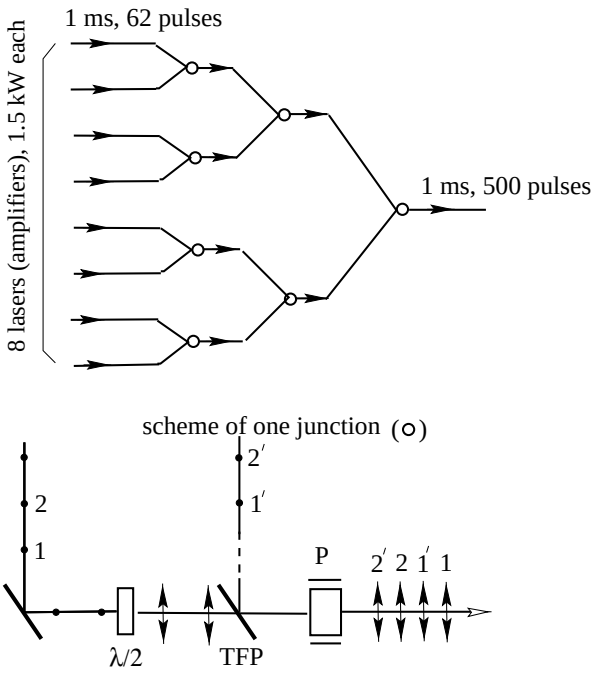

Figure 2.4: *The laser system required for the storage ring.*

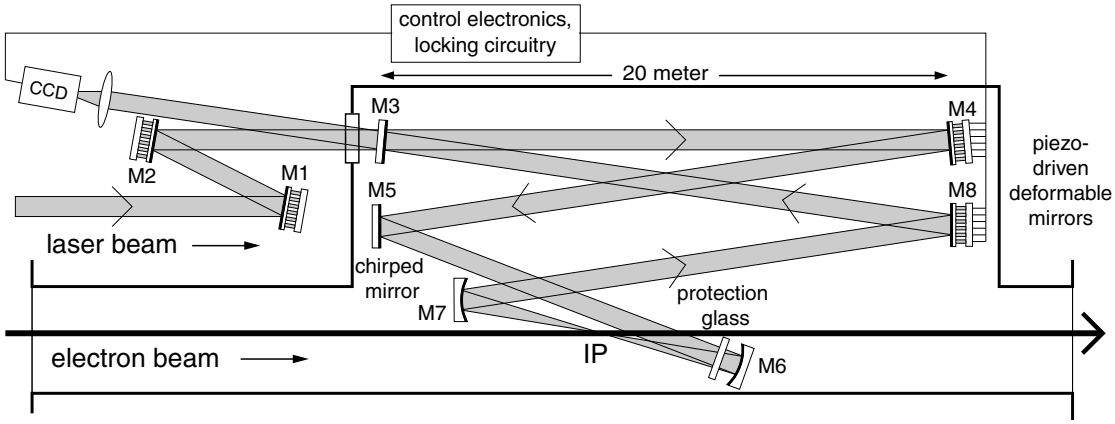

Figure 2.5: *The optical cavity.*

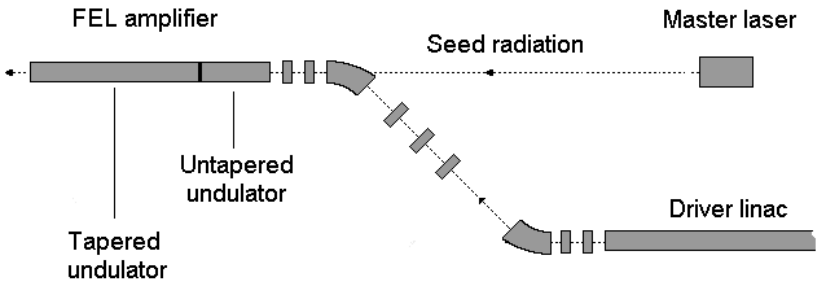

Figure 2.6: *The Free Electron Laser.*

Free Electron Laser: Yet another way to obtain the required laser parameters is to use a FEL, see Figure 2.6. The FEL is composed of a driver linac, a master laser and an undulator magnet. After acceleration, the electrons are directed to the undulator and exposed to the laser pulse from the master laser. In the undulator, the electron trajectory is altered by the magnets, producing synchrotron radiation, which amplifies the laser pulse. This radiation will have the same pulse structure as the electrons in the driver linac, which of course have the same structure as the electron bunches in TESLA. The advantage with the FEL, apart from the fact that it delivers short pulses with high energy, is that all technologies are already developed for the main TESLA project, which includes an X-ray facility with a self-amplified spontaneous emission FEL. However, it still requires one additional accelerator, so this option might be more advantageous for linear accelerators with $\sqrt{s} > 800$ GeV, where longer laser wavelenghts are needed.

$\sqrt{s}$	*500*	*800*
$N_{e/bunch}/10^{10}$	2	2
$N_{bunches/train}/10^3$	3	3
τ_{bunch} $[ps]$	1.5	1.5
τ_{train} $[ms]$	1	1
$f_{rep,bunches}$ $[MHZ]$	3	3
$f_{rep,trains}$ $[HZ]$	5	5
σ_z $[mm]$	0.3	0.3
$\sigma_{x/y}$ $[nm]$	88/4.3	69/3.4
b $[mm]$	2.1	2.7
λ_L $[\mu m]$	1.06	1.06
E_{flash} $[J]$	5	5
$f_{rep,laser}$ $[kHZ]$	14.1	14.1
P_{av} $[kW]$	140	140

Table 2.1: *Parameters for the photon collider and the laser system for two c.m. energies.* $\sigma_{x,y,z}$ *is the size of the beam, where the z-axis is in the beam direction.*

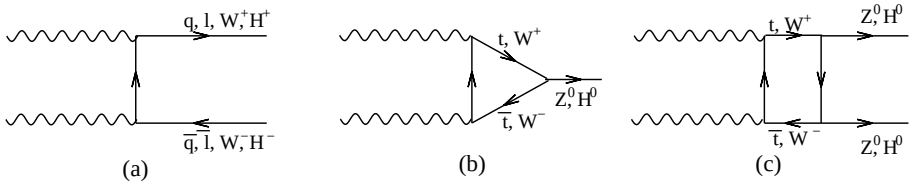

Figure 2.7: *The production of particles in $\gamma\gamma$ collisions.*

2.3.3 $\gamma\gamma$-physics

The production of charged particles in $\gamma\gamma$ collisions is, in a first approximation, due to direct coupling, see Figure 2.7a. In these processes, any charged particle can be produced (assuming the c.m. energy is high enough). Since photons only couple to electrically charged particles, neutral particles are produced via loops of charged particles, see Figure 2.7b,c. Many of these reactions can also be produced in e^+e^- collisions, but there are some advantages of using $\gamma\gamma$ collisions; for example, the cross section for pairs of scalars, fermions or vector particles are all about one order of magnitude larger in $\gamma\gamma$ collisions. Also, in many cases the $\gamma\gamma$ cross secions increase with $\sqrt{s}$, while the corresponding cross sections for e^+e^- collisions decrease with $\sqrt{s}$. Due to the much higher cross sections, the particle production rate will in most cases be higher in $\gamma\gamma$ collisions, although the luminosity is somewhat smaller. In addition, the production of pairs of charged particles is, in lowest order, a pure QED process, in contrast to the corresponding e^+e^- processes, which also depend on the weak charge of the produced particles.

The Higgs mechanism

In the Standard Model, the mass of the elementary particles is generated by the Higgs mechanism, and associated with this is the Higgs boson. In the SM there is only one Higgs boson and the present data indicates that it is lighter than 200 GeV. If this is correct, it is likely to be discovered at the existing hadron collider TEVATRON or at the LHC. Precise measurements of its mass, lifetime, production cross section etc. could then be done at TESLA and the Photon Collider to decide whether this particle is the SM Higgs or if it is one of the at least five supersymmetric (SUSY) particles predicted by various SUSY theories. One advantage with the photon collider is that the photon polarisation can be controlled, making it possible to explore the particles charge-parity properties very efficiently. The heavy Higgs bosons H and A in the Minimalistic SUSY extension of the SM (MSSM) [2] may however not be discovered at the LHC, and in e^+e^- collisions, H and A can only be produced in pairs. Since they can be very heavy, up to about 1 TeV, and are expected to have very similar masses, the TESLA e^+e^- mode can in the initial phase ($\sqrt{s} = 500$ GeV) only produce these if they have masses up to about 250 GeV. The $\gamma\gamma$ mode, on the other hand, can produce these particle singly up to masses of about 400 GeV (with the upgraded c.m. energy $\sqrt{s} = 800$ GeV, the mass limit will be about 660 GeV). The MSSM also predics two heavy charged Higgs bosons, H^+ and H^-, which, at an energy corresponding to the maximum cross section, can be produced by $\gamma\gamma \rightarrow H^+H^-$ with a production rate almost one order of magnitude higher than in the e^+e^- mode. The photon collider should also be able to distingush between a SM Higgs and a Higgs predicted by other theories, like Next-to MSSM and the two Higgs Doublet Model (2HDM) [3].

Hints of the electroweak symmetry breaking (the Higgs mechanism in the SM) may be found in a change of the couplings for W^+, W^- and Z^0. Hence, precision measurements of the processes $\gamma\gamma \to W^+W^-$ and $\gamma e \to \nu W$ would be an important part of the TESLA project. Deviations from SM predictions may also be seen in anomalous top quark couplings.

Supersymmetry
In addition to (at least) five Higgs bosons, SUSY also predicts that all particles in the SM have a supersymmetric partner, for example photino ($\tilde{\gamma}$), sfermions ($\tilde{f}$), squarks ($\tilde{q}$) and gluinos ($\tilde{g}$). Since we do not see these particles in nature, it is assumed that this supersymmetry is broken. Just as with the SM, no one has found a way to predict the masses theoretically, but with certain assumptions, one can constrain the masses. Some of these particles will be produced in e^+e^-- and $\gamma\gamma$-collisions if the particles have masses within the kinematical range, but the production rates will be larger in $\gamma\gamma$-collisions at TESLA energies. Also, selectrons ($\tilde{e}$) and neutralinos ($\tilde{\nu}$) may be produced most efficiently in γe-processes and the bound state of two stop quarks, stoponium ($\tilde{t}\tilde{t}$), may be formed in $\gamma\gamma$-reactions. The lightest SUSY particle may be stable and could therefore be a candidate for the Dark Matter that is believed to exist in the Universe.

String theories and extra dimensions
In some theories, called string theories, the particles are assumed to be small strings, and not mathematical points as in conventional quantum field theory. The aim of these theories is to unify gravitation and quantum theory. In string theories, extra dimensions are predicted to exist (in addition to our ordinary 3+1 dimensions) in which gravity can propagate. As a consequence, gravity should become strong at the Planck scale ($\sim 10^{19}$ GeV), but some of these theories predict that gravity becomes strong already at a few TeV. Such effects could be observed as deviations from the SM predictions of cross section and angular distribution in $\gamma\gamma \to W^+W^-$, and, with smaller search reach, in $e^+e^- \to f\bar{f}$.

Probing the photon
The quark and gluon distribution in the photon can be measured in $\gamma\gamma$ processes like $\gamma\gamma \to Q\bar{Q}X$, where $Q\bar{Q}$ is either a charm or beauty quark pair. The cross section of this process is sensitive to the gluon content in the photon because of the subprocesses $\gamma g \to Q\bar{Q}$ and $gg \to Q\bar{Q}$, see Chapter 3. Moreover, if polarised photons are used, also the spin dependent structure functions of the photon can be measured. It is also important to understand the $\gamma\gamma \to Q\bar{Q}$ process, since it will be background to the Higgs decay $H \to Q\bar{Q}$.

2.4 Detectors

In order to make a correct analysis of the processes in the collisions, one needs to identify the particles involved as well as measure their momenta and energies. The basic structure of modern detectors used in high energy physics is more or less the same for all experiments, why this short presentation, based on the TESLA detector at the linear e^+e^- collider, also can be applied for the detectors at LEP and the $\gamma\gamma$ collider. In fact, the detector for the $\gamma\gamma$ collider will be very much the same as for the e^+e^- mode, except that a laser system must

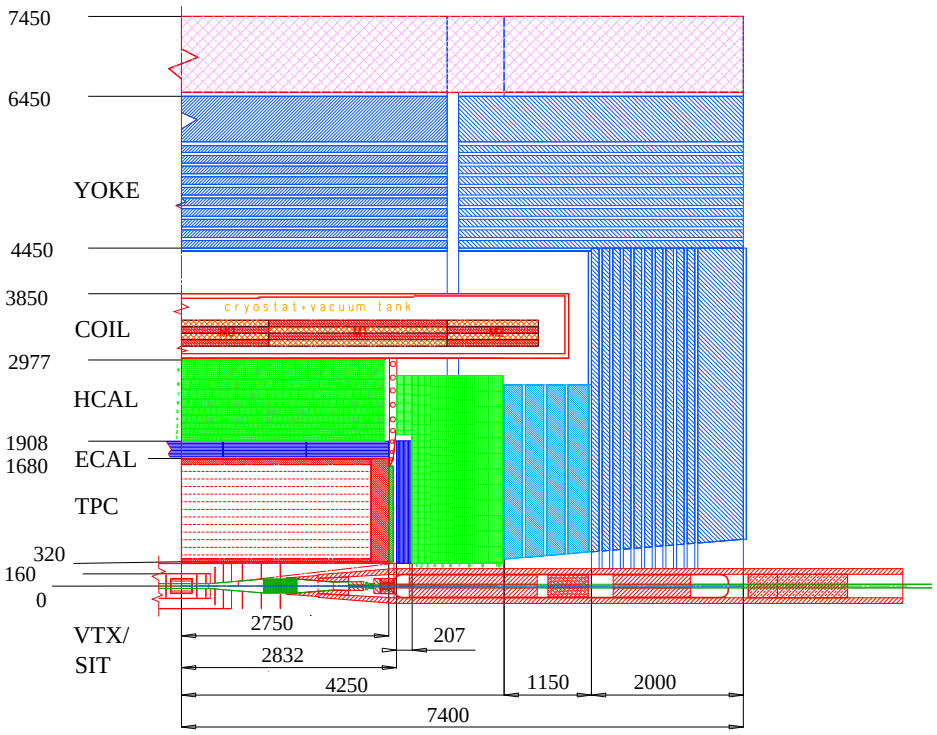

Figure 2.8: *A side view of one quadrant of the TESLA detector. Also shown are the dimensions (in mm) of the different parts.*

be implemented in the $\gamma\gamma$ detector. A more detailed description of the TESLA detector can be found in [4].

2.4.1 The tracking system

Figure 2.8 shows a side view of one quadrant of the TESLA detector. As seen, the detector is built up of different layers, from the tracking system closest to the beampipe to the outermost muon system. The tracking system (see Figure 2.9) consists of the vertex detector (VTX) and the intermediate (SIT), forward (FTD and FCH), and central (TPC) tracking chambers. When charged particles move through the tracking detectors, they ionize the material, and this ionization can be detected and reconstructed as points on a particle track. Since the whole detector is surrounded by a 4 T magnet, the particles will be bent in different directions depending on the charge, and the radius of curvature will give information about the momentum.

The vertex detector
Since many particles produced in high energy collisions have very short lifetimes, and thus travel a very short distance before decaying, a vertex detector is needed to distinguish particles that are produced in the direct collision from the daughter particles of decayed particles. Also, with the vertex detector, the collision point can be reconstructed. For TESLA, the vertex detector will be optimized for reconstruction of b and c decays, in order to detect final states with many b or c quarks like ZHH and $t\bar{t}H$, and also to separate $H \to b\bar{b}$ from $H \to c\bar{c}$.

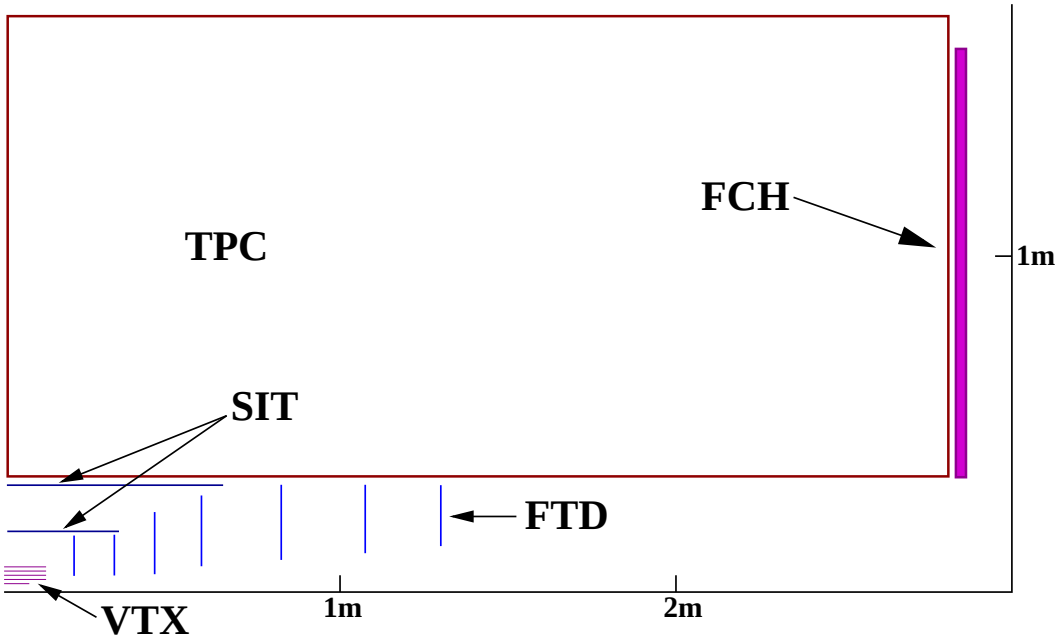

Figure 2.9: *A side view of one quadrant of the tracking system.*

The intermediate and forward tracking system
The SIT will consist of double sided silicon strip detectors formed as a cylinder, and will give a resolution of about 50 μm. The FTD will consist of seven layers, where the first three are pixel detectors with a pixel size of 50×300 μm^2. The other four will, like the SIT, consist of strip detectors with a resolution of about 25 μm. The precise measurements of these detectors will improve the momentum resolution and also link the tracks in the vertex detector to the tracks found in the central tracking chamber.

The central tracking chamber
In order to get a good track resolution and reconstruction, many points have to be measured along the track. Therefore, the time projection chamber (TPC), which is one of the two central tracking chambers, is very large. The TPC is a cylindrical chamber with inner and outer radii 320 mm and 1700 mm, respectively, containing a three component gas mixture. When the charged particles move through the TPC, they ionize the gas, creating free electrons which drift towards the endplates because of the electric field inside the TPC. These electrons also ionize the gas, creating a cascade of secondary electrons which are detected as a current at the endplates. By measuring the time between the passage of the particle and the detection of the electrons at the endplate, the exact position of the particle can be calculated, since the drift velocity of the electrons is known. The TPC is complemented by a forward tracking chamber (FCH). The FCH consists of straw chambers positioned at both ends of the TPC, and are also filled with a gas mixture, giving a resolution of about 50 μm.

2.4.2 The calorimeter system

The energies of the particles are measured by the calorimeters, in which the particles deposit all their energy by interacting with the absorber material and thereby creating particle

showers. These showers then interact with the active material, creating photons or electrical charge, which are detected. For photons and electrons, the relevant processes are pair creation and bremsstrahlung while hadrons create particle showers via strong interaction with the core of the absorber atoms. The calorimeter system at TESLA consists of four parts: the central electromagnetic and hadronic calorimeters, and two forward calorimeters.

The electromagnetic calorimeter

The EM calorimeter (ECAL) is the innermost of the four parts. Here, all particles that interact through the EM force, like electrons, positrons and photons, are detected. At TESLA, there are two options for the ECAL: a shashlik calorimeter and a SiW calorimeter. The shashlik ECAL consists of towers of alternating absorber (Pb) and scintillating plates, where each plate is 1 mm thick. The light from the scintillating plates is extracted by wavelenght shifting fibres, which are connected to the tower by longitudinal holes through the stock. The SiW calorimeter consists of tungsten (W) absorbers and silicon (Si) pads, arranged in the same basic structure as the shashlik calorimeter. When the particles move through the silicon pads, they create an electric charge, which is measured. Because of the high density of tungsten, the transverse size of the showers will be smaller and the EM showers can more easily be separated from the hadronic ones. The SiW ECAL would therefore give a better performance than the shashlik option, but would also be much more expensive.

The hadronic calorimeter

Whereas electrons and photons are fully absorbed in the ECAL, hadrons continue through it and are eventually absorbed in the hadronic calorimeter (HCAL), which is located behind the ECAL, as seen from the interaction point. Also here, there are two options for the TESLA detector: the Fe/scintillating tile calorimeter and a digital calorimeter. The former is, like the ECAL, made of scintillator plates subdivided in tiles, and the light from these tiles is collected by fibres and transported to the readout. The tiles will be 5×5 cm^2 in the inner layer and increase to 25×25 cm^2 in the outer layer. The other option is to use the same construction as the tile HCAL above, but divide the tiles in 1 cm^2 cells. The signal from these cells would be purely digital, and to estimate the energy, one can simply count the number of cells with energy deposited. The high granularity of this digital option would match the SiW ECAL very well.

The forward calorimeters

The calorimeter system is complemented by two forward calorimeters in order to cover as large a solid angle as possible. This is very important, since some processes are characterised by missing energy, for example where neutrinos, or more exotic particles like SUSY particles, are part of the final state. The Low Angle Tagger (LAT) and the Luminosity Calorimeter (LCAL) both extend the ECAL, covering angles down to 30 mrad and 6 mrad respectively. The LCAL will also act as a luminosity detector, so the beams can be tuned properly. Moreover, it will shield the rest of the detector from backscattered particles and synchrotron radiation. It is estimated that the LCAL will be hit by $2 \cdot 10^4$ electron-positron pairs, carrying over 20 TeV, per bunch crossing. Despite their small size, these detectors

will heavily increase the overall detector performance.

2.4.3 The coil and muon system

The coil provides a solenoidal field of 4 T along the z-axis, i.e. along the beam direction. The field, as aready mentioned, bends the charged particles, allowing momentum measurements. The outermost detector system, the muon system, allows identification of cosmic muons and muons created in the collisions. This is necessary since muons can travel through a lot of material without being absorbed. The cosmic muons can be used for calibration of the detector, since the track should be a straight line. The muon system is also used to detect hadrons that has not deposited all their energy in the calorimeters.

Chapter 3

Heavy quark production

The production of heavy flavour (b and c quarks) in $\gamma\gamma$ collisions has been studied at LEP [5, 6, 7, 8, 9, 10, 11, 12, 13, 14] for many years and will be an important field of study at TESLA. It has also been studied in proton-photon collision at HERA [15, 16, 17, 18, 19, 20], and in proton-proton collisions at the TEVATRON [21, 22, 23, 24]. Whereas the measured charm cross sections are well described by the parton evolution according to the standard collinear approach, which will be discussed later in this chapter, the measured beauty cross sections are a factor 2-4 larger than predictions. However, by using so called k_t-factorization and an unintegrated gluon density for the proton, the beauty cross sections are now in good agreement with data in pp collisions [25, 26]. The aim of this thesis is to investigate if the $b\bar{b}$ cross section also can be explained in $\gamma\gamma$ collisions by using k_t- factorization and an unintegrated gluon density for the photon.

3.1 Kinematics

In heavy quark production one can define the Lorenz invariant variables Q^2, y, x_{Bj}, s and W^2. In the case of e^+e^- collisions, as in LEP, these variables can be expressed with the four-momenta of the incoming and outgoing electrons, P_1, P_2, P_3 and P_4, see Figure 3.1. If we let q_1 be the four-momentum of the photon we can define the virtuality of the photon as

$$Q_1^2 \equiv -q_1^2 = -(P_1 - P_3)$$

where $Q_1^2 > 0$, since $q_1^2 < 0$. q_1 is called a spacelike momentum, since q_1^2 is negative[1]. The virtuality is related to the square of the transverse momentum of the photon, $Q^2 = \frac{p_t^2}{1-y}$, where y is defined in (3.2), and is thus also related to the wavelength of the photon, $Q^2 \propto \frac{1}{\lambda^2}$. The virtuality therefore describes the resolving power of the photon, since λ has to be of the same order or smaller than the size of the object that shall be resolved. We

[1]This is a consequence of the conservation of four momentum, and that the electron is considered massless.

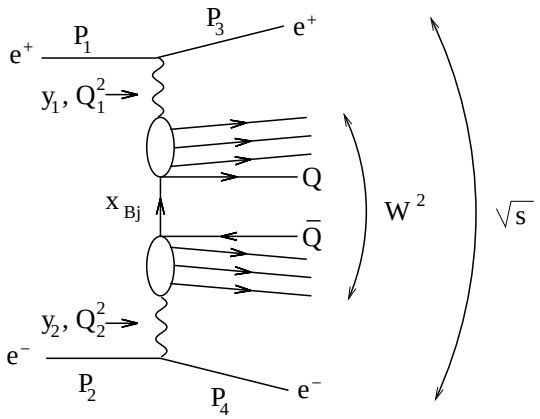

Figure 3.1: *Kinematic variables in $\gamma\gamma$ collisions.*

can also define the fraction x_{Bj} of the electron momentum carried by the parton in the quark box and the fraction y of the electron energy carried by the photon as

$$x_{Bj} \equiv \frac{q_1^2}{2 \cdot P_2 \cdot q_1} \tag{3.1}$$

and

$$y_1 \equiv \frac{P_2 \cdot q_1}{P_2 \cdot P_1}. \tag{3.2}$$

The momentum fraction carried by a parton in general is labeled x. The invariant mass squared of the hadronic final state system can be written as

$$W^2 = (q_1 + q_2)^2,$$

and similarly, the c.m. energy $\sqrt{s}$ is given by

$$s = (P_1 + P_2)^2.$$

In the $\gamma\gamma$ collider at TESLA, all photons are real in contrast to the e^+e^- collisions at LEP where the photons are virtual. Hence, in the $\gamma\gamma$ collider $Q^2 = 0$. In this case, y has no meaning, and there is no general definintion for x_{Bj}. Also, all final state particles belong to the hadronic final state, so

$$W^2 = s = (q_1 + q_2)^2.$$

3.2 The structure of the photon

It is well known that the proton not only consists of three valence quarks, but also of virtual gluons that hold the quarks together. These gluons can split up in quark-antiquark pairs, called sea quarks, which in turn can emit gluons, see Figure 3.2a. A photon colliding

with a proton may therefore interact either with one of the valence quarks or with one of the sea quarks.

In analogy with the proton, a photon can be seen as a flux of virtual quarks and gluons. However, the photon does not consist of any valence quarks, and must first fluctuate into a virtual quark-antiquark pair which can emit gluons, see Figure 3.2b. When a photon interacts with a virtual quark in another photon, the former is said to resolve the latter. How much of the photon that is resolved depends on the virtuality Q^2 of the resolving photon, as described in the previous section. So, what a photon with a low Q^2 will resolve as a quark, a photon with a higher Q^2 might resolve as a quark and a gluon which is radiated by the quark, sharing the original quark momentum. A photon with a very high Q^2 may also resolve the soft gluon as having split up in a quark-antiquark pair. This means that the more we resolve the more quarks we see at smaller x, since each daughter particle must have less momentum than the mother. The density of quarks and gluons thus depends on Q^2, a phenomenon called scaling violation. This is described by the density function $f_i(x, \mu^2)$ which is just the probability that a parton of type i (quark or gluon) is carrying a longitudinal momentum fraction x of the photon, at a scale $\mu^2 = Q^2$. The scale is generally denoted μ^2, since it does not always have to be the virtuality of the photon that sets the scale. The structure function for the whole photon can then be written as

$$F_2^\gamma(x, \mu^2) = x \sum_i e_i^2 f_i(x, \mu^2)$$

where e_i is the electric charge of parton i and one sums over all quark flavours. Of course, the photons cannot interact with the gluons, since $e_{gluon} = 0$, and F_2^γ does not depend on the gluon structure function explicitly (in LO and DIS NLO [27]). However, since the quark density at small x is driven by the gluon density, it is possible to extract $f_{gluon}(x, \mu^2)$. In general, the cross section that a parton i from one photon will interact with a parton j from another photon and form the final state X is

$$\sigma = \sum_{i,j} \int \frac{dx_1}{x_1} \frac{dx_2}{x_2} \cdot F_i^\gamma(x_1, \mu^2) \cdot F_j^\gamma(x_2, \mu^2) \cdot \hat{\sigma}_{i+j \to X}(M^2, x_1, x_2, s) \tag{3.3}$$

where the structure functions describe the probability of finding partons i and j with momentum fractions x_1 and x_2 and the constituent cross section $\hat{\sigma}$ describes the probability that the two particles i and j will create the final state X. The constituent cross section is proportional to the square of a Matrix Element (ME), which in turn depends on the masses, virtualities, couplings etc. of the particles involved. The integral is over all x_1 and x_2 allowed by the kinematics. Unlike the constituent cross section, the structure functions cannot be calculated from first principles. Instead, experimental fits and phenomenological methods must be used in order to describe the parton distributions inside the photon.

3.3 k_t-factorization

All factors in equation (3.3) above only depend on the longitudinal momentum fraction x and the scale μ^2. This means that all partons are assumed to travel in the same direction as the incoming particle, i.e. they have no transverse momenta. It is therefore called a

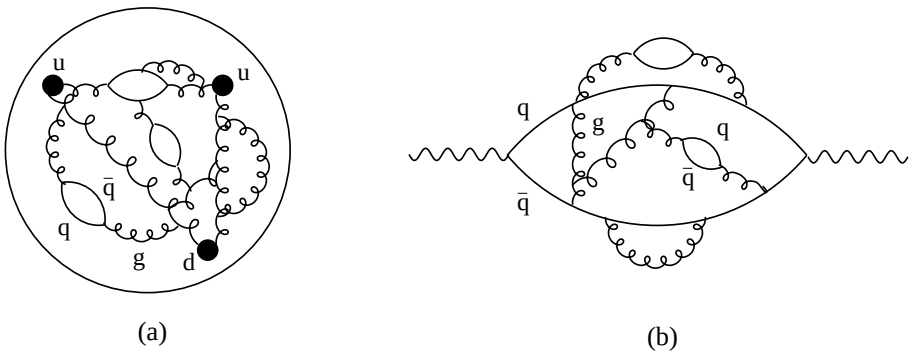

(a) (b)

Figure 3.2: *The structure of the proton (a) and the photon (b).*

collinear approximation. However, at large energies, where small x gluons are probed, the transverse momenta k_t of the partons are expected to be important. Therefore, the cross sections are factorized into a k_t-dependent (off-shell) constituent cross section $\hat{\sigma}(x, k_t^2, \mu^2)$ and a k_t-dependent parton density function $\mathcal{A}(x, k_t^2, \mu^2)$. The equivalent to equation (3.3) then becomes

$$\sigma = \sum_{i,j} \int \frac{dx_1}{x_1} \frac{dx_2}{x_2} dk_{t1}^2 dk_{t2}^2 \mathcal{A}_i^\gamma(x_1, k_{t1}^2, \mu^2) \mathcal{A}_j^\gamma(x_2, k_{t2}^2, \mu^2) \hat{\sigma}_{i+j \to X}(k_{t1}, k_{t2}, M^2, x_1 x_2 s). \quad (3.4)$$

The function $\mathcal{A}(x, k_t^2, \mu^2)$ is called the (k_t-) unintegrated gluon density and is related to the collinear one by

$$g(x, \mu^2) \simeq \int_0^{\mu^2} dk_t^2 \mathcal{A}(x, k_t^2, \mu^2), \quad (3.5)$$

where $\mathcal{A}(x, k_t^2, \mu^2)$ describes the probability to find a gluon with a longitudinal momentum fraction x and a transverse momentum k_t at a scale μ^2. Inverting the relation (3.5) gives that an unintegrated gluon density may be obtained by differentiating an integrated gluon density with respect to μ^2,

$$\mathcal{G}(x, k_t^2) = \left. \frac{dg(x, \mu^2)}{d\mu^2} \right|_{\mu^2 = k_t^2} \quad (3.6)$$

Note that the unintegrated gluon density obtained in this way only depends on one scale, since $\mu^2 = k_t^2$. To distinguish the different parton distributions, the following notation is used: $g(x, \mu^2)$ is the parton distribution in the collinear approach, while $\mathcal{G}(x, k_t^2)$ and $\mathcal{A}(x, k_t^2, \mu^2)$ are the one- and two-scale distributions in the k_t-factorization approach. When using off-shell matrix elements of leading order ($O(\alpha_s)$), some next-to leading order ($O(\alpha_s^2)$) processes in the collinear approach are effectively included, in addition to all collinear leading order processes.

3.4 Heavy quark production processes

Heavy quark production in photon collisions can be explained by three mechanisms, shown in Figure 3.3. At small $\sqrt{s}$, the cross section is dominated by the direct part (1). In this

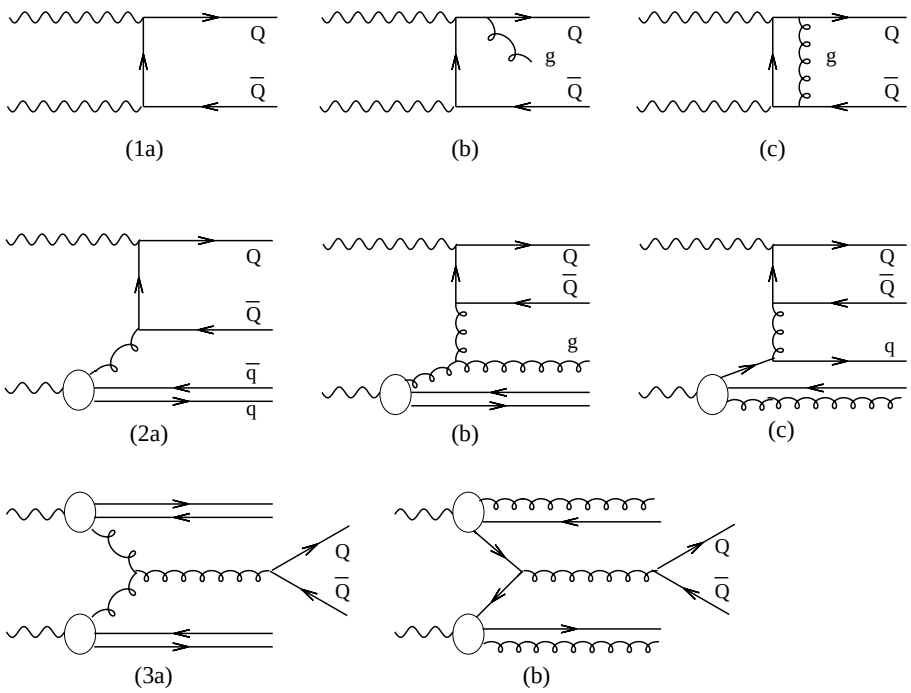

Figure 3.3: *Production mechanisms in heavy quark production.*

case, the photons couple directly to the quarks, and the process is therefore not dependent on the quark and gluon content in the photon. Hence, the lowest, or zeroth, order process (1a) can be calculated in pure QED, while first order corrections, including real (1b) and virtual (1c) gluon radiation, also depend on the QCD coupling constant. These corrections have been calculated in [28] and were found to contribute 30% of the cross section in the direct case. It has also been shown that the direct part alone (including corrections) cannot reproduce the measurements of b and c quark production in e^+e^-, ep and pp collisions.

In the single resolved case (2), one of the photons splits up in a flux of quarks and gluons, where one of these gluons fuse with the other photon. The next-to-leading order corrections are shown in 2b and c. Since this process depends on the quark and gluon distribution in the photon, it cannot be calculated using perturbative QCD, but must be treated phenomenologically. The direct and single resolved processes are predicted to give equal contributions to the cross section at $\sqrt{s} \approx 200$ GeV [28]. In 3a and b is shown the double resolved case, where both photons split up and create a heavy quark pair. This process gives a smaller contribution than the direct and first resolved processes, since it depends on $\alpha^2 \approx 0.014$, but it becomes increasingly important with increasing energy.

3.5 Higher order processes

The processes in Figure 3.3 are all of zeroth, first or second order in the strong coupling α_s, and the matrix elements have all been calculated using perturbative QCD. However, in high energy collisions it is possible to have many gluon emissions, making the zeroth, first and even second order calculations insufficient to decribe the data. Due to the self coupling of

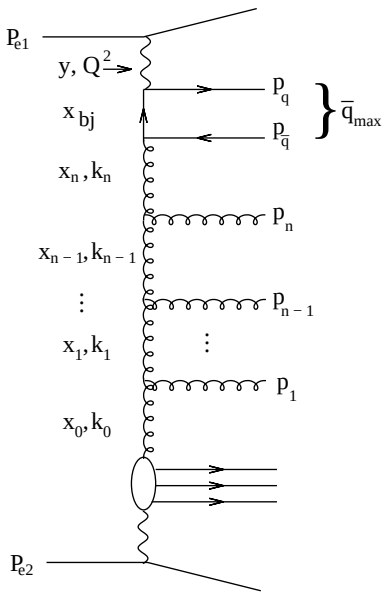

Figure 3.4: *Parton ladder created by gluon emissions.*

the gluons, the complexity of the processes increases rapidly with increasing order, making perturbative calculations very difficult. Instead one uses evolution equations to generate the higher order emissions. These equations describe, under certain approximations, how a mother parton is split into two daughter partons, one of which is emitted whereas the other continues as a propagator parton. The daughter propagator parton is then split into two daughters and so on. This creates a parton ladder, as illustrated in Figure 3.4. The general structure of an evolution equation is

$$f_j = f_0 + \int f_i \cdot P_{i \to j,k}$$

where f_i and f_j are the parton density functions for the mother and daughter propagator gluons, f_0 is the input gluon density function and $P_{i \to j,k}$ is the splitting kernel describing the probability that the parton i is split into two partons j and k. In the following discussion, the evolution starts at the bottom in Figure 3.4 and continues towards the quark box. The possible splittings are $q \to qg$, $g \to q\bar{q}$ and $g \to gg$. There are a number of different evolution equations, each one taking different parts of the expansion of $P_{i \to j,k}$ into account and evolving the density functions in different variables. A short presentation of three different approaches follows, where the first is valid for large μ^2, the second is valid for small x and moderate μ^2, and the third is valid for both these regions. The latter is of special importance for this thesis.

3.5.1 The DGLAP evolution

The DGLAP [29, 30, 31, 32] evolution equation is of the form

$$\frac{df_j(x,\mu^2)}{d\ln\mu^2} = \frac{\alpha_s(\mu^2)}{2\pi} \sum_i \int_x^1 \frac{dx'}{x'} f_i(x',\mu^2) P_{i \to j,k}(z) \tag{3.7}$$

where $f(x,\mu^2)$ is the density of partons carrying a longitudinal momentum fraction x probed at a scale μ^2, and $P_{i\to j,k}(z)$ describes the probability that a parton i is split into two partons j and k with a fraction $z = \frac{x}{x'}$ and $1-z$ of the original parton momentum, respectively. The probability that a gluon splits into two gluons is given by

$$P_{g\to g,g}(z) = \frac{1}{1-z} - 2 + z(1-z) + \frac{1}{z} \tag{3.8}$$

where the terms $\frac{1}{1-z}$ and $\frac{1}{z}$ are called the singular terms, since they give infinite contributions when $z \to 1$ and $z \to 0$, respectively. The equation (3.7) thus describes the probability change of finding a parton of type j with momentum fraction x as we increase the scale μ^2. This is the scaling violation mentioned in Chapter 3.2. In the DGLAP formalism, the gluon chain in Figure 3.4 is assumed to be strongly ordered in virtuality

$$\mu^2 \gg |k_n^2| \ldots \gg |k_1^2| \gg |k_0^2|, \tag{3.9}$$

where k_i is the four momentum of parton i. This means that in each splitting $i \to i+1, j$ one can approximate $k_0^2 = k_1^2 = \ldots\ k_i^2 = 0$ compared to k_{i+1}^2, and since $k_i^2 = m_i^2$ these partons are considered to be massless (or on-shell). It can be shown that the ordering in virtuality implies that also the transverse momentum of the propagator partons are strongly ordered (at small z) according to

$$\mu^2 \gg |k_{tn}^2| \ldots \gg |k_{t1}^2| \gg |k_{t0}^2| \tag{3.10}$$

where $k_{ti} = (0, k_{xi}, k_{yi}, 0)$. Hence, in each splitting one can approximate $k_{t0}^2 = k_{t1}^2 = \ldots\ k_{ti}^2 = 0$, which means that the DGLAP approach is a collinear approximation (which is obvious since there is no k_t-dependence in (3.7)). It can be shown, that using the DGLAP evolution is equivalent to resum terms of the form $(\alpha_s \ln(\mu^2))^n$ in the expansion of the cross section. Hence, the DGLAP approximation is only valid at large μ^2 where these terms will dominate.

3.5.2 The BFKL evolution

The BFKL [33, 34, 35] evolution equation resums the terms $(\alpha_s \ln(\frac{1}{x}))^n$ in the expansion, and is thus only valid at small x and moderate μ^2. It is of the form

$$\frac{d\mathcal{G}(x,k_t^2)}{d\ln(\frac{1}{x})} = \int dk_t'^2 \mathcal{G}(x,k_t'^2) \cdot K(k_t^2, k_t'^2). \tag{3.11}$$

Here, the function K is the splitting kernel equivalent to P in (3.7). The evolution is made in increasing $\ln(\frac{1}{x})$, since

$$x_0^2 \gg x_1^2 \ldots \gg x_n^2 \gg x_{Bj}^2 \tag{3.12}$$

has been assumed. This implies that the emitted gluons will take a large fraction of the propagator momentum. However, there is no ordering in k^2 or k_t^2, so the collinear approximation can not be used, and the matrix elements must be taken off-shell (the particles can have a virtual mass). Another important consequence of this is that unintegrated parton densities must be used in (3.11), i.e. they must depend on k_t.

3.5.3 The CCFM evolution

The CCFM [36, 37, 38, 39] evolution equation is valid both at large and small x, since it resums terms of both the form $(\alpha_s \ln(\frac{1}{x}))^n$ and $(\alpha_s \ln(\frac{1}{1-x}))^n$. This means that at large x the CCFM evolution will be DGLAP-like, and at small x it will be BFKL-like. The CCFM evolution includes angular ordering in the initial state cascade, which means that the emission angles of the partons with respect to the propagator increases as one moves towards the quark box,

$$\Xi \gg \xi_n \gg \dots \xi_1 \gg \xi_0, \tag{3.13}$$

where the maximum allowed angle Ξ is set by the hard quark box,

$$p_q + p_{\bar{q}} = \Upsilon(P_{e1} + \Xi P_{e2}) + \vec{Q}_t.$$

This is written in the Sudakov variables, where p_q, $p_{\bar{q}}$, P_{e1} and P_{e2} are the four momenta of the produced heavy quarks and the incoming particles, respectively (see Figure 3.4), Υ and $\Upsilon\Xi$ are the positive and negative light-cone momentum fractions of the heavy quark pair, and $\vec{Q}_t$ is the sum of the transverse momentum vectors of the heavy quark pair. The momenta of the emitted gluons can be written similary,

$$p_i = v_i(P_{e1} + \xi_i P_{e2}) + p_{ti},\ \xi_i = \frac{p_{ti}^2}{s v_i^2},$$

where $v_i = (x_{i-1} - x_i)$ is the momentum fraction of the emitted gluon, p_t is the transverse momentum of the gluon, and $s = (P_{e1} + P_{e2})^2$ is, as usual, the squared center of mass energy. Here, we have assumed that all particles are massless. The CCFM equation is written as

$$\bar{q}^2 \frac{d}{d\bar{q}^2} \frac{x\mathcal{A}(x, k_t^2, \bar{q}^2)}{\Delta_s(\bar{q}^2, \mu_0^2)} = \int dz \frac{d\phi}{2\pi} \frac{\tilde{P}(z, k_t^2, (\bar{q}/z)^2)}{\Delta_s(\bar{q}^2, \mu_0^2)} x' \mathcal{A}(x', k_t'^2, (\bar{q}/z)^2)$$

where

$$\bar{q}_i = \frac{p_{ti}}{1 - z_i} = x_{i-1}\sqrt{s\xi_i}$$

is the rescaled transverse momenta of the emitted gluons and $z_i = \frac{x_i}{x_{i-1}}$. In this formalism, (3.13) becomes

$$q_i > z_{i-1} q_{i-1}. \tag{3.14}$$

When $z \to 1$ we have $q_i > q_{i-1}$, i.e. ordering in rescaled transverse momentum, which means that the evolution is DGLAP-like. In the limit $z \to 0$ the angular ordering gives no restrictions on the rescaled transverse momentum. Also, (3.12) holds because of the definition of z. This means that the evolution is BFKL-like. The Sudakov form factor Δ_s describes the probability that there are no emissions from the starting scale μ_0^2 to the maximum angle $\bar{q}_{max}^2$. The CCFM splitting function $\tilde{P}$ is defined as

$$\tilde{P}_g(z, k_t^2, (\bar{q}/z)^2) = \frac{\bar{\alpha}_s(q_i^2(1 - z_i)^2)}{1 - z_i} + \frac{\bar{\alpha}_s(k_{ti}^2)}{z_i} \Delta_{ns}(z_i, k_{ti}^2, q_i^2), \tag{3.15}$$

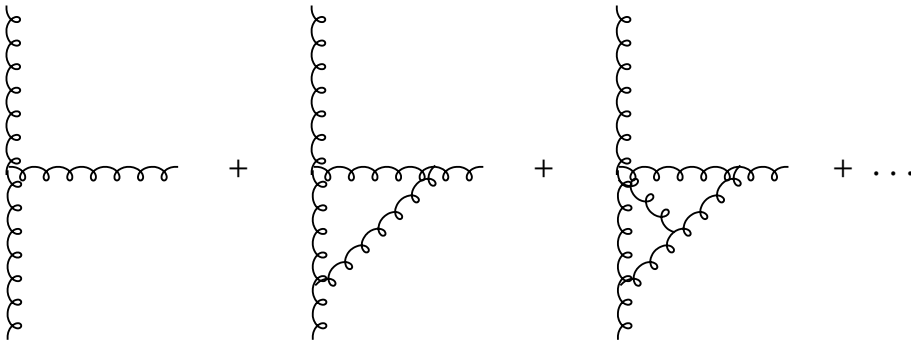

Figure 3.5: *The Reggeization of the gluon vertex.*

which is somewhat different than the DGLAP splitting function (3.8). First of all, the CCFM splitting function only includes the singular parts of the DGLAP splitting function. The other difference is that there is one additional function Δ_{ns}, called the non-Sudakov form factor, in (3.15). The non-Sudakov form factor originates from the fact that, in CCFM and BFKL, all virtual corrections in the gluon vertex are automatically taken into account, see Figure 3.5. This is called the Reggeization of the gluon vertex.

3.6 Monte Carlo simulations

As was already mentioned, higher order processes are very difficult to calculate using perturbative QCD. Moreover, it is not quarks that are detected in the experiments, but hadrons. The transition from parton level (Figure 3.3, for example) to hadron level takes place over long distances where α_s is large. Hence, perturbation theory is not valid here. To overcome this problem, Monte Carlo (MC) generators are used. For each event, these programs generate all the particles, their four-momenta and all the kinematic variables according to certain theoretical prescriptions. The higher order gluon emissions are simulated by evolving the parton ladder according to some evolution equation (DGLAP, BFKL, CCFM etc.), and the transitions to hadron level can also be implemented via hadronization models.

3.6.1 CASCADE

The Monte Carlo generator CASCADE [40] is based on the CCFM evolution equation and thus uses unintegrated parton desities and off-shell matrix elements. For technical reasons, a backward evolution is used, where first the hard scattering is generated and then the initial state cascade (the gluon ladder) is evolved from the quark box to the incoming particles. In this evolution only gluon emissions are treated, that is, only the splitting $g \to gg$ is considered. CASCADE also performs the hadronization, using the Lund string model in JETSET/PYTHIA [41].

3.6.2 The Monte Carlo method

The Monte Carlo method is often used when one wants to integrate difficult expressions or generate random numbers according to complicated functions. Assume one wants to generate random numbers according to the disribution $f(x)$, and that this function is complicated. Then one can generate two random numbers R_1 and R_2 instead; R_1 according to a simple function $g(x)$ which includes $f(x)$, and R_2 uniformly between 0 and 1. By only choosing the R_1 values which satisfies

$$f(R_1) > R_2 \cdot f_{max}, \tag{3.16}$$

where f_{max} is the maximum value of the function $f(x)$ in the considered interval, the R_1 values will be generated according to the function $f(x)$ (see Figure 3.6).

Now assume one wants to integrate the function $f(x)$ over a region V. The Monte Carlo theorem then states that

$$\int f dV \approx \frac{V}{N} \sum_{i=1}^{N} f(x_i). \tag{3.17}$$

So, instead of performing the actual integration, which can be difficult if $f(x)$ is complicated, one can instead pick N random points $x_1, x_2, \ldots, x_N$ uniformly in the region V, then calculate $f(x_i)$ for each x_i and use (3.17) above. If V has a complicated shape, it can be difficult to sample these points. Then, one can instead sample the points in a region W, which includes V, and set

$$f(x_i) = 0$$

for all x_i that lie outside the region V (which is just a variation of (3.16) above). Of course, one should choose the region W as close to V as possible, since the points that are not used increases the error. The error can also be decreased if the random points are not chosen uniformly, but according to a function $g(x)$, say, that includes $f(x)$, and $g(x) \sim f(x)$. This is especially important if the function $f(x)$ is peaked, since the points outside the peak will have a small effect on the estimate of the integral, but will increase the error. With this method, the estimate of the integral is more based on the important points, and the method is therefore called importance sampling, see for example [44] for a detailed description.

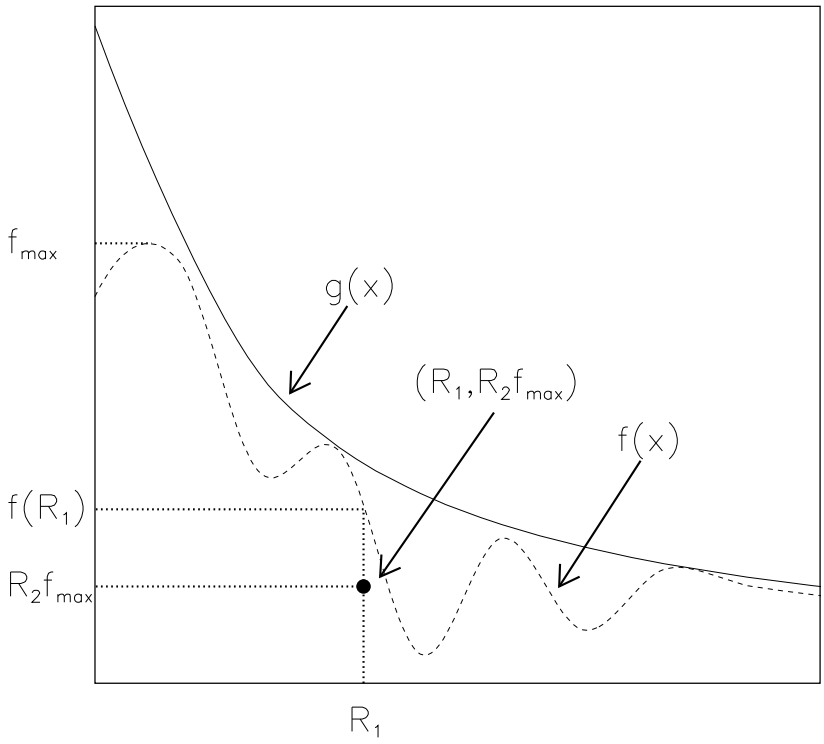

Figure 3.6: *The Monte Carlo technique of generating random numbers according to a complicated distribution $f(x)$ by generating random numbers according to a simple function $g(x)$, see text. In this example, the random number R_1 is accepted since $(R_1, R_2 f_{max})$ lies below the $f(x)$ curve.*

Chapter 4

The unintegrated gluon density

In this chapter, the evolution machinery is tested using the one-loop (DGLAP-like) evolution for the proton and the photon. Then, the unintegrated gluon density for the photon is obtained using the full CCFM evolution, and the uncertainties in the evolution are discussed. Since the distributions obtained with the CCFM evolution were compared with the derivative of standard gluon density functions, taken from [42], a short discussion of the differentiation method will be given first.

4.1 Numerical differentiation method

Two numerical differentiation methods were tested: DDERIV [43] and DFRIDR [44], which are based on Rombergs principle of sequence extrapolation and Richardson's deferred approach to the limit, respectively. The first test was to differentiate the simple function $f(x) = -\frac{1}{x}$ with respect to x. Here, both methods gave good results, but only after adjusting a parameter in DDERIV. A second test was to differentiate the GRV[1] [45] density function with respect to the scale μ^2, then to integrate over k_t^2 and compare the results with the original GRV distribution. This was done because we will later use that

$$\mathcal{G}(x, k_t^2) = \frac{d}{d\mu^2} g(x, \mu^2) \Big|_{\mu^2 = k_t^2} \tag{4.1}$$

which relates the unintegrated parton density function $\mathcal{G}(x, k_t^2)$ to the integrated one $g(x, \mu^2)$. The adaptive Gaussian method taken from [46] was used for the integration. As seen in Figure 4.1, the DFRIDR routine reproduced the distribution succesfully, except in the high x region which will be discussed later. However, with the same value of the parameter as used above, the DDERIV approach gave unacceptable results, and only after changing this parameter again the obtained distribution (which is shown in the figure) started to resemble the original one. Because of this poor reproduction of the input distribution, and its sensitivity to the choice of parameter, we decided to use DFRIDR instead of DDERIV.

[1] GRV-G-HO was used.

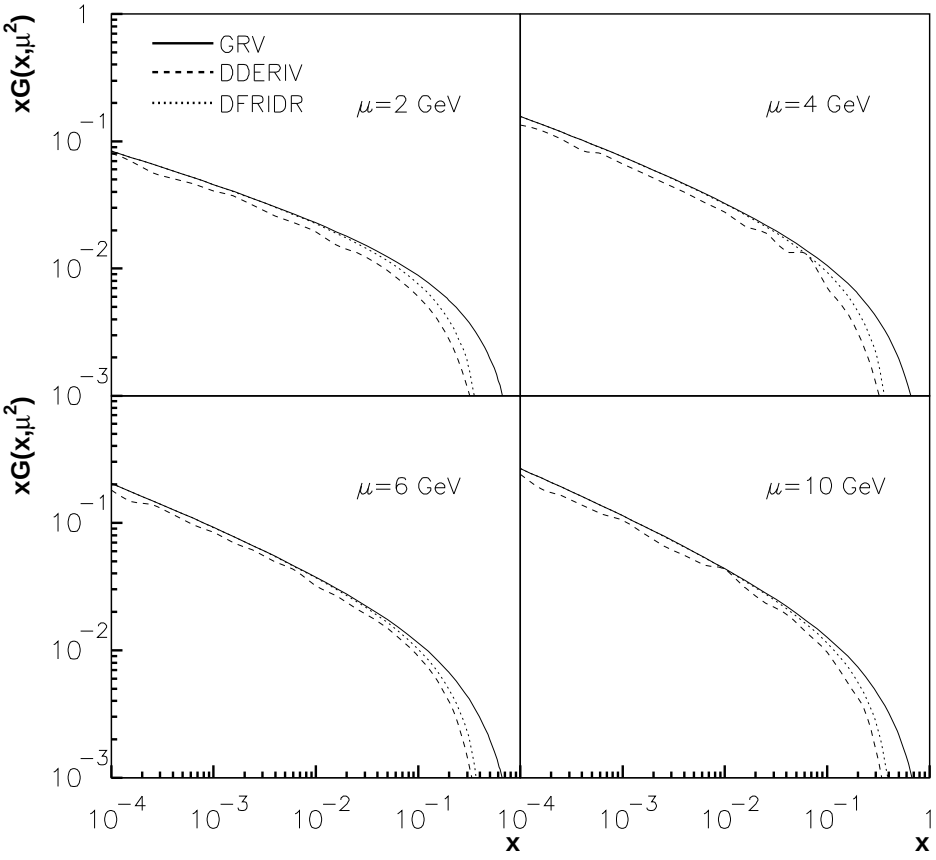

Figure 4.1: *The GRV distribution differentiated with DFRIDR and DDERIV, and then integrated, compared with the original GRV distribution.*

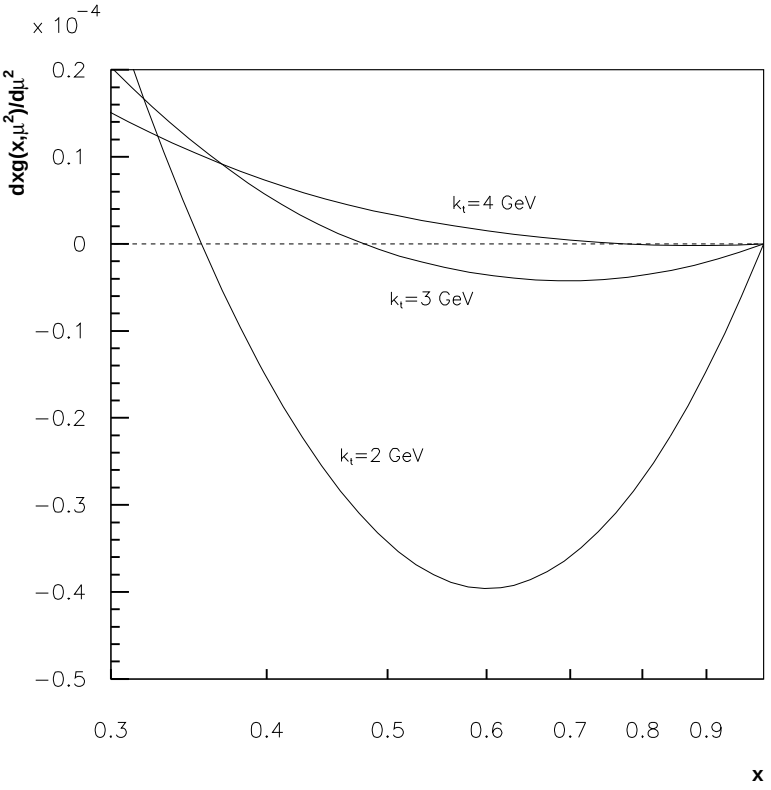

Figure 4.2: $\mathcal{G}(x, k_t^2)$ *as a function of* x *for different values of* $\mu = k_t$. *When the function becomes negative, the differentiation method of obtaining the unintegrated gluon density becomes invalid.*

The deviations from the original distribution at high x is due to the fact that the function (4.1) becomes negative in this region. This is because of the scaling violation: as the scale μ^2 increases, smaller distances are resolved and as a consequence we resolve more gluons with small x (i.e. $x < 0.1$) and less gluons with high x. In Figure 4.2 is shown how the point, where the derivative becomes negative, changes with $\mu = k_t$. The smallest x-value for this point is obtained with $k_t = 2$ GeV, where $x \approx 0.35$. Since $\mathcal{G}(x, k_t^2)$ is interpreted as a probability, the method becomes invalid at such high x.

4.2 Evolution of the unintegrated gluon density

The evolution of the unintegrated gluon density was made using the CCFM equation in a forward evolution procedure based on the Monte Carlo technique as described in [47]. An initial gluon distribution is chosen as well as a starting scale μ_s and an emission angle $\bar{q}_s$ for the first emitted gluon. The default values $\mu_s = \bar{q}_s = 1.4$ GeV was obtained by a fit to the proton structure function [47]. The evolution then starts with $\bar{q}_{max,0} = \bar{q}_s$, and k_{t0} chosen from a Gaussian distribution around μ_s to simulate a Fermi motion of the partons. x_0 is chosen from the initial gluon distribution using the Monte Carlo method. The branching is then repeated until the next emitted gluon would have a higher emission angle than $\bar{q}_{max,0}$. This is repeated 10^7 times for each of the 50 different maximum angles $\bar{q}_{max,i}$ chosen from

$\bar{q}_{max,0} = \bar{q}_s < \bar{q}_{max,i} < \bar{q}_{max,50} = 1800$ GeV in steps of $log(\bar{q}_{max})$, thus giving a distribution $\mathcal{A}(x, k_t^2, \bar{q})$ in a $50 \times 50 \times 50$ grid of $log(x)$, $log(k_t^2)$ and $log(\bar{q}_{max})$. For values between the gridpoints the method of linear interpolation is used. With the unintegrated parton distribution avaliable, a backward evolution scheme can be used for the simulation of the parton emissions.

4.3 One-loop evolution

To make sure that the evolution procedure is working, the evolution was first made for the proton with a GRV[2] input distribution (using the default values $\mu_s = \bar{q}_s = 1.4$ GeV) and using the one-loop approximation, which means that the CCFM evolution is reduced to the DGLAP evolution, with the difference that the CCFM one-loop evolution still treats the full kinematics, i.e. it takes the transverse momentum k_t into account. This is done by putting $\Delta_{ns} = 1$ in the splitting function (3.15) and reducing the condition (3.14) to ordering in transverse momentum (3.10). The obtained distribution $x\mathcal{A}(x, k_t^2, \bar{q})$ was then integrated over k_t^2,

$$\int_0^{\bar{q}} dk_t^2 \, x\mathcal{A}(x, k_t^2, \bar{q}) = x\mathcal{G}(x, \bar{q}), \tag{4.2}$$

and compared to the original GRV distribution at different scales, see Figure 4.3. The small differences are due to the fact that the splitting function only contains the singular parts, and that only the splitting $g \to gg$ is considered. Nevertheless, the distributions are still in good agreement which indicates that the evolution machinery is working.

The situation for the photon is a bit different, since the structure function, in addition to the hadronic component, now also consists of a pointlike component which reflects the splitting of the photon into a quark-antiquark pair. Also, there are no sum rules equivalent to those in the proton case that constrain the quark distributions in the photon. However, these differences do not matter, since we only use the gluon distribution and the gluon splitting $g \to gg$. Figure 4.4 shows the evolved distribution for the photon, using the same parameters as in the proton case and the GRV[3] as input distribution, compared to the input distribution at different scales. The one-loop evolved and the GRV distributions show a similar behaviour, although the one-loop evolved distribution is a bit steeper at large scales. It is not surprising that the one-loop evolution does not give equally good agreement in the proton and the photon case, since the same parameters have been used in both one-loop evolutions, while different techniques and starting scales for the proton and the photon were used to obtain the original GRV distributions.

From the above we conclude that the one-loop evolution is able to reproduce the input distributions reasonably well, and hence that the evolution machinery is working for the CCFM one-loop case. A similar test cannot be done for the full CCFM evolution, since the obtained distributions should be different from the ones obtained with DGLAP evolution. However, it has already been shown [47] that the CCFM evolution is working for the proton, in the sense that it can explain data, for example $b\bar{b}$ production at the TEVATRON,

[2]GRV 98 HO was used
[3]GRV-G HO was used

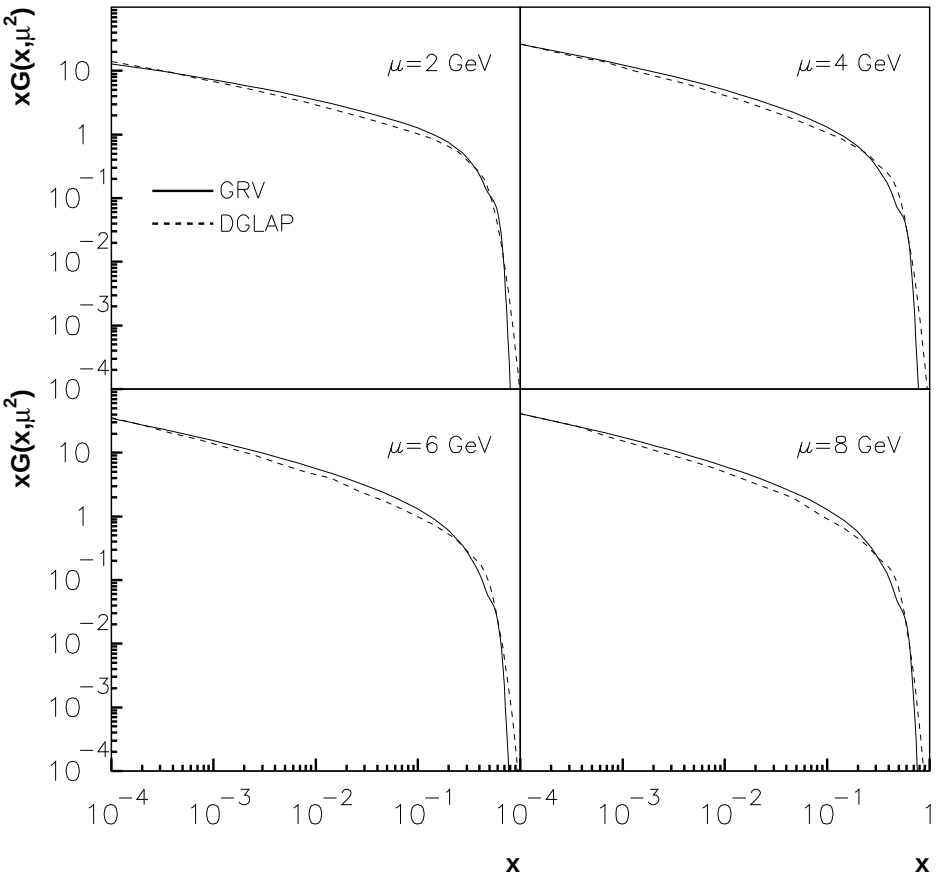

Figure 4.3: *The integrated DGLAP evolved distribution for the proton compared to the GRV distribution at different scales.*

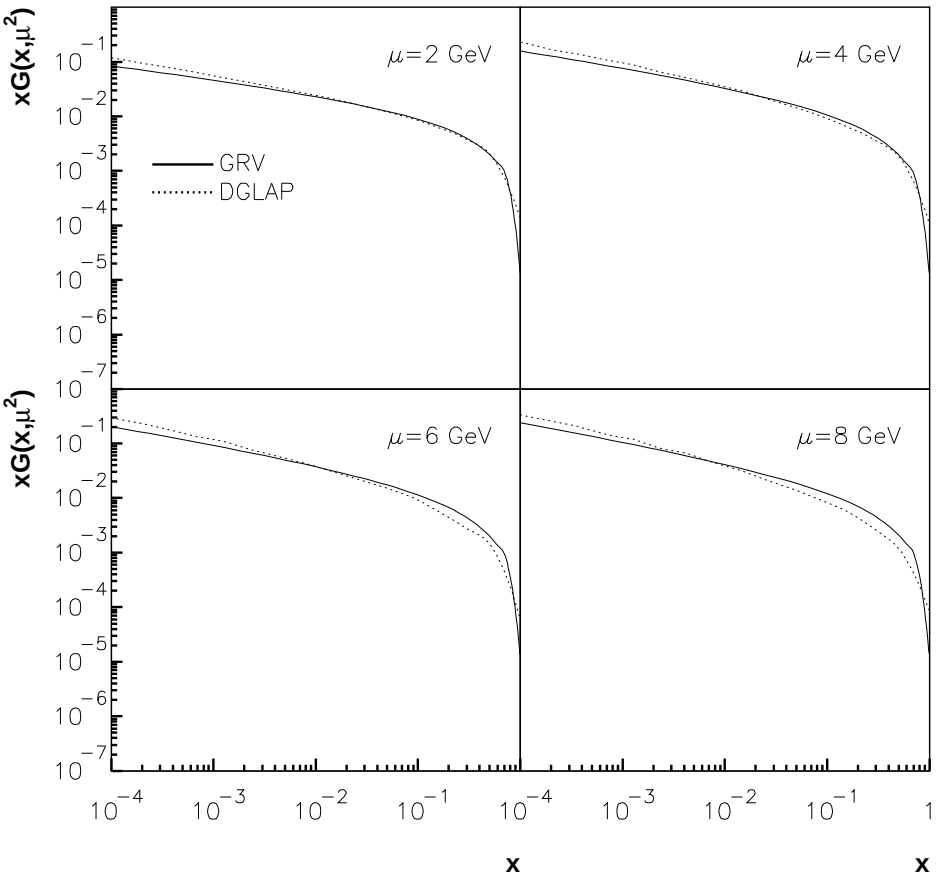

Figure 4.4: *The integrated DGLAP evolved distribution for the photon compared to the GRV distribution at different scales.*

which could not be explained with other methods. Since the only difference between the photon and proton evolution is the starting distribution, it can be assumed that the CCFM evolution will work also for the photon.

4.4 CCFM evolution

After making sure that the parton evolution scheme gives consistent results, the unintegrated gluon density for the photon was evolved using the full CCFM evolution procedure. The obtained distributions integrated over k_t^2 are compared in Figure 4.5 to the GRV[4] distribution, which was used as input distribution. One of the more obvious differences is that the CCFM evolved distribution is much higher than the original GRV. This is due to differences in the definition of the integrated gluon density; one can either integrate over d^2k_t or over dk_t^2. The difference is a factor π, which explains the main part of the normalization difference. We can also note that the CCFM evolved distribution is less steep than the original GRV. This is a consequence of that the non-Sudakov form factor $\Delta_{ns} \to 0$ when $z \to 0$ and thereby screens the $\frac{1}{z}$ factor in the splitting function. This results in a lower splitting probability compared to the DGLAP case (where $\Delta_{ns} = 1$) which becomes visible in the small x (small z) region where the factor $\frac{1}{z}$ dominates the splitting function.

In Figure 4.6 is shown the unintegrated distribution as a function of x for different values of k_t, and as a function of k_t^2 for different values of x, compared to the derivative of GRV. Here, $\mu = \bar{q} = 10$ GeV. Also in Figure 4.6a we see that the CCFM distribution in general is higher (except at very high k_t) and we can also see the non-Sudakov supression at small x. We should also remember that the derivative method becomes invalid at high x because $\frac{dg(x,\mu^2)}{d\mu^2}$ becomes negative. This explains the big difference between the CCFM evolved distribution and the GRV at $k_t = 2$ GeV, because the derivative becomes negative already at $x \approx 0.35$ (see Figure 4.2). In Figure 4.6b one can see the typical exponential k_t-dependence of the derivative of GRV. Since the GRV distribution is only defined for $\mu^2 = k_t^2 \geq 0.3$ GeV^2, it is replaced with $\frac{x\mathcal{G}(x,k_{t0}^2)}{k_{t0}^2}$ for $k_t^2 < k_{t0}^2 = 0.3$ GeV^2 [48]. We can also note that the probability for the gluons to have a $k_t^2 > \mu^2 = 100$ GeV^2 in the CCFM approach is significant, which would not be possible using DGLAP. This is a consequence of the k_t^2-ordering in the DGLAP evolution, where k_t^2 is always less than μ^2, see (3.10), and the non-ordering in k_t^2 in the CCFM evolution, where the gluons can have any kinematically allowed value of k_t^2.

4.5 Uncertainties

In the evolution of the unintegrated gluon distributions above, the GRV density was used as input distribution, with $\mu_s = \bar{q}_s = 1.4$ GeV given from a fit to the parton density of the proton [47]. A natural question is how sensitive the results are to the selected starting distribution and the parameters chosen. Therefore, the evolution was made also with the SaS[5] [49] parton distribution as input (and keeping $\mu_s = \bar{q}_s = 1.4$ GeV), and

[4]GRV-G HO was used

[5]SaS-G 1D was used

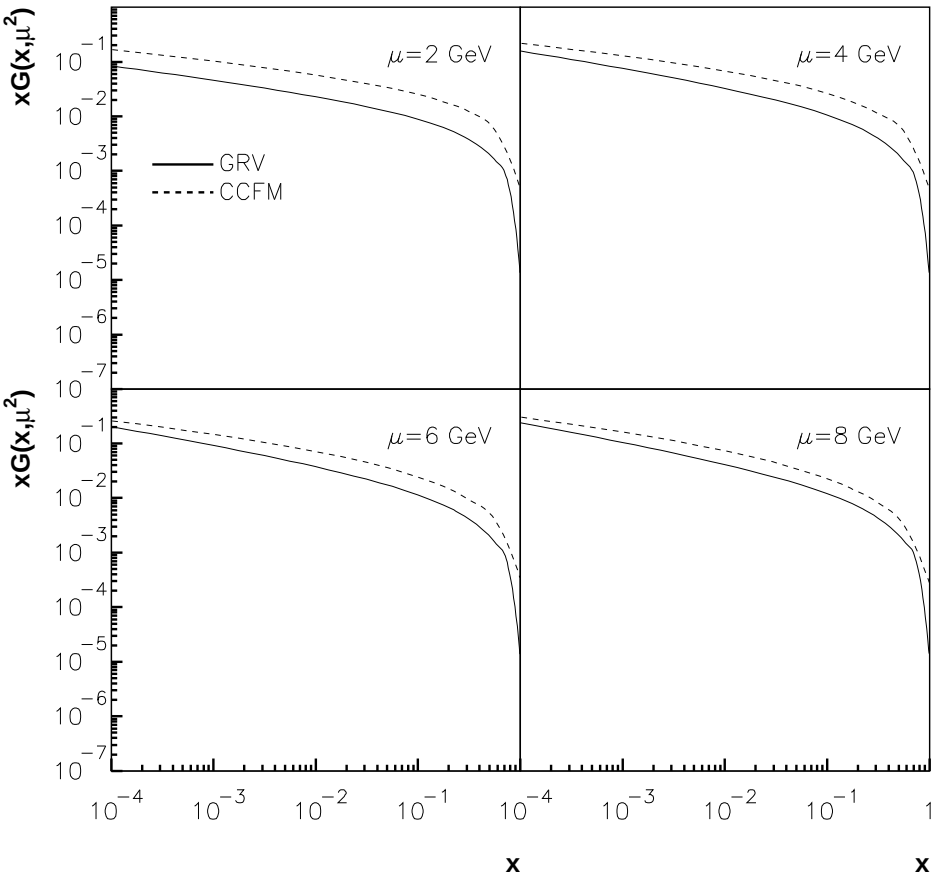

Figure 4.5: *The integrated CCFM evolved distribution for the photon compared to the GRV distribution at different scales.*

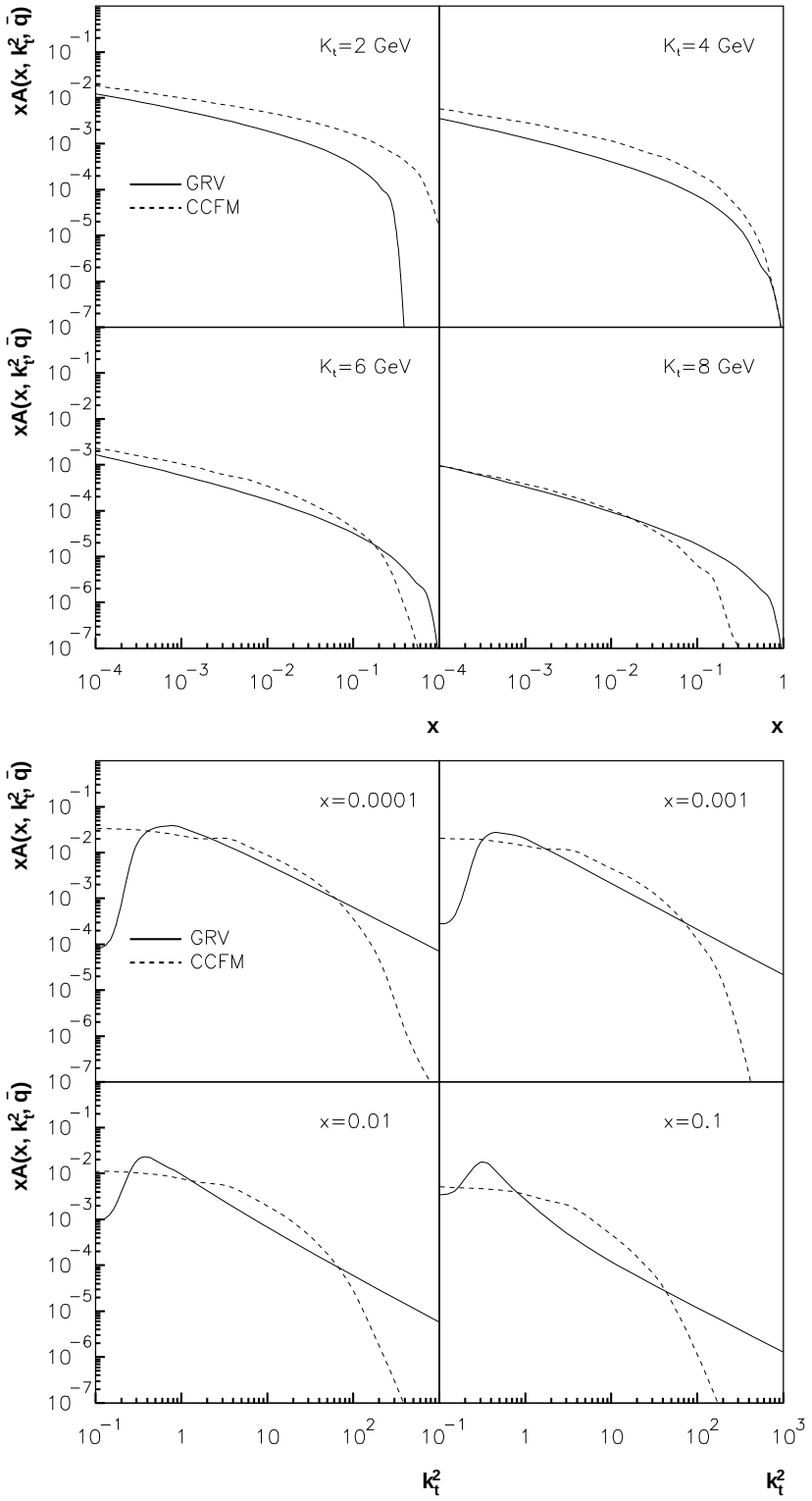

Figure 4.6: *The unintegrated CCFM evolved distribution for the photon compared to the derivative of the GRV distribution as a function of x for different values of k_t (a), and as a function of k_t^2 for different values of x (b).*

also with the GRV parametrization as input but with $\mu_s = 1.4$ GeV and $\bar{q}_s = 1.2$ GeV, $\mu_s = 1.4$ GeV and $\bar{q}_s = 1.6$ GeV, and $\mu_s = 1$ GeV and $\bar{q}_s = 1.4$ GeV. The various distributions obtained are compared to the previous ones in Figure 4.7 and 4.8. When comparing the integrated distributions, see Figure 4.7, we see that there is only a weak dependence on the starting angle $\bar{q}_s$, such that the distribution becomes somewhat flatter at large $\bar{q}_s$. This can be understood, since a larger starting angle would mean that it takes less emissions to reach the maximum value (since there is angular ordering), and less emissions would mean that the gluon entering the matrix element (gluon n in Figure 3.4) would have a larger longitudinal momentum fraction x. A change in μ_s makes a significant difference, where a smaller μ_s gives a distribution which is lower at small x. One can also see that the evolution depends on the choice of input distribution, where the main features of the input distribution remains after the evolution, see also Figure 4.9.

Also when comparing the unintegrated gluon densities in Figure 4.8, we see that the dependence on $\bar{q}_s$ is small while changing μ_s makes a significant difference, especially in the region $1 < k_t^2 < 10$. This is probably due to details in the evolution: In order to avoid soft emissions a cut-off scale μ_s is defined. Thus if the propagator gluon has $k_t > \mu_s$ a real emission is allowed, but it is not if $k_t < \mu_s$. Since there is no ordering in k_t in the CCFM evolution any propagator gluon along the evolution chain might get $k_t < \mu_s$ after a real emission. In that case, the evolution of the propagator is continued until $k_t > \mu_s$ and a real emission is allowed.

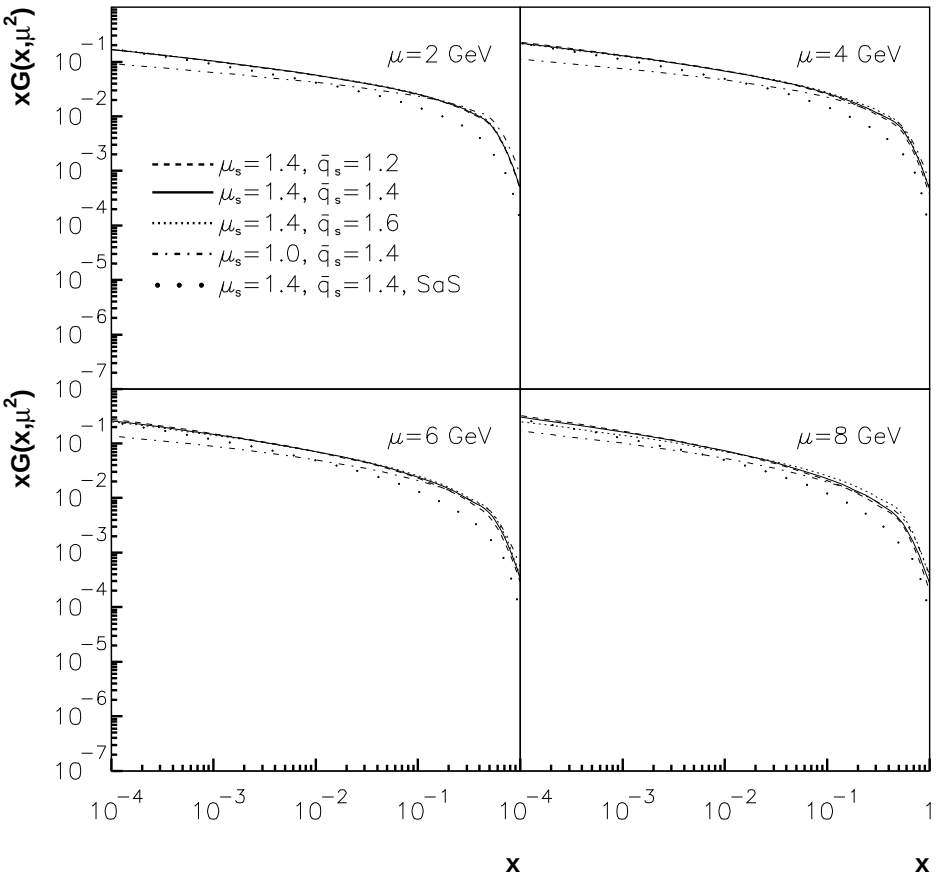

Figure 4.7: *The integrated CCFM evolved distributions for the photon with different combinations of μ_s, $\bar{q}_s$ and input distributions.*

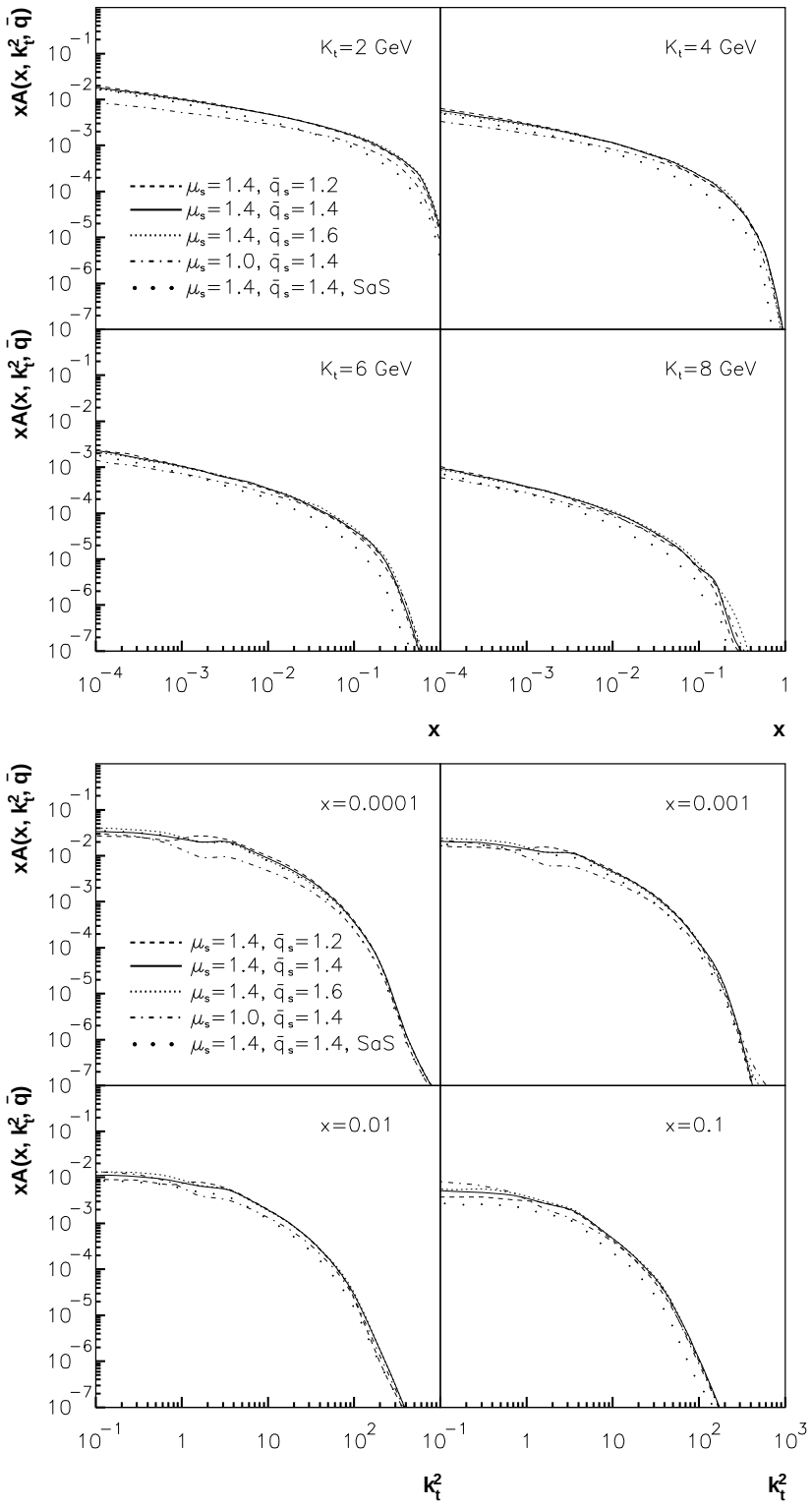

Figure 4.8: *The unintegrated CCFM evolved distributions for the photon with different combinations of μ_s, $\bar{q}_s$ and input distributions.*

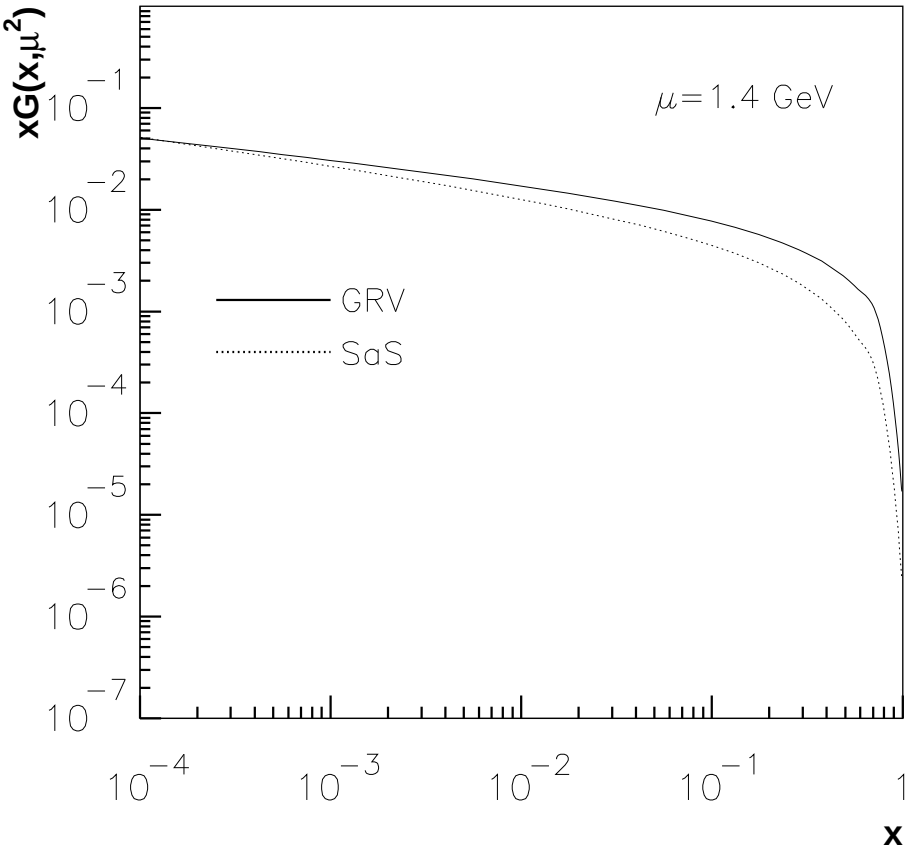

Figure 4.9: *The GRV and SaS distributions compared at the starting scale* $\mu = 1.4$ *GeV.*

Chapter 5

Heavy quark cross sections

In this chapter, the unintegrated gluon density obtained in Chapter 4 is used as an input to the MC generator CASCADE to calculate heavy quark cross sections in e^+e^- collisions, which are compared to LEP data. Also, predictions for heavy quark cross sections in e^+e^- and $\gamma\gamma$ collisions at TESLA energies are given.

5.1 Cross section calculation test

The direct and single resolved cross sections for b and c quark production in e^+e^- collisions were calculated with CASCADE and compared with the results in [28]. Since the direct cross section is independent of the gluon content in the photon, and hence independent of evolution equations, these cross sections should agree. In heavy flavour production, CASCADE uses off-shell matrix elements as calculated in [50]. Errors were found in [50] (eq. B16) where a factor $N_c e_q^2$ was missing in the direct cross section ($N_c = 3$ being the color factor and e_q being the EM charge of the produced quarks). With these factors taken into account, the direct cross sections from CASCADE and from leading and next-to-leading order calculations [28] were in good agreement, see Table 5.1. For the single resolved case, the DGLAP evolution was used with the gluon density according to GRV[1] to describe the photon structure and with cuts and parameters as in [28]. As seen, also these cross sections where in good agreement. This shows that the basic machinery for cross section calculations in CASCADE is working.

5.2 e^+e^- cross sections at LEP

The e^+e^- cross sections can be calculated using the relation

$$\sigma_{e^+e^-\to e^+e^- b\bar{b},c\bar{c}X} = \int \frac{dQ_1^2}{Q_1^2}\frac{dQ_2^2}{Q_2^2}\mathcal{L}_{\gamma\gamma}(W_{\gamma\gamma}, Q_1^2, Q_2^2)\sigma_{\gamma\gamma\to b\bar{b},c\bar{c}X}(W_{\gamma\gamma})dW_{\gamma\gamma} \qquad (5.1)$$

[1] GRV-G 1HO was used, as in [28]

CHARM

$\sqrt{s}$	$\sigma_{DIR}(pb)$		$\sigma_{1-RES}(pb)$	
(GeV)	*DREES*	*CASCADE*	*DREES*	*CASCADE*
180	296.8 (396.3)	328	269.9 (305.8)	217
91.2	191.2 (254.8)	213	93.38 (109.5)	80

BEAUTY

$\sqrt{s}$	$\sigma_{DIR}(pb)$		$\sigma_{1-RES}(pb)$	
(GeV)	*DREES*	*CASCADE*	*DREES*	*CASCADE*
180	1.280 (1.582)	1.35	1.371 (1.644)	1.19
91.2	0.663 (0.823)	0.71	0.302 (0.371)	0.27

Table 5.1: *Direct and single resolved charm and beauty cross sections calculated with CASCADE and compared to leading and next-to-leading order (in parenthesis) calculations in [28] (DREES). Here,* $\mu^2 = 2m^2$, $\Lambda = 0.34$ *GeV,* $m_b = 4.75$ *GeV and* $m_c = 1.6$ *GeV. In CASCADE, the scale factor 0.5 was used to obtain the correct scale.*

where $\mathcal{L}_{\gamma\gamma}$ is the photon flux in the electron, $W_{\gamma\gamma}$ is the center of mass energy in the $\gamma\gamma$ system, Q_i is the virtuality of photon i and $\sigma_{\gamma\gamma\to b\bar{b},c\bar{c}X}$ is the cross section for the subprocess $\gamma\gamma \to b\bar{b}, c\bar{c}X$. No cuts were made, i.e. all kinematically allowed processes were considered.

In Figure 5.1 are shown the obtained cross sections for b and c quark production in e^+e^- collisions calculated with the k_t-factorization approach, using off shell ME and a CCFM unintegrated gluon density evolved from a starting distribution given by GRV, compared to the collinear (DGLAP) predictions and data [5, 6, 11, 12, 13, 14]. Here, the masses $m_b = 4.5, 4.75, 5$ GeV and $m_c = 1.3, 1.5, 1.7$ GeV were used for the CCFM cross sections, while $m_b = 4.75$ GeV and $m_c = 1.5$ GeV were used for the cross sections calculated with DGLAP. This variation of the quark masses gives an estimate of the uncertainty in the calculation (see the discussion of uncertainties in Chapter 5.4). One can see that the k_t-factorization approach describes the charm data reasonably well and that it gives larger cross sections compared to the collinear method. One can also see that the choice of mass makes a significant difference, such that a smaller mass gives a larger cross section. Nevertheless, the cross sections obtained with 1.3 GeV$< m_c <$ 1.7 GeV all lie within the experimental uncertainties.

The cross sections for $b\bar{b}$ production, on the other hand, are not well described. However, in the CCFM approach, one has to determine carefully the normalization of the cross sections. The reason for this is that the normalization of the unintegrated gluon density does not have to be the same as for the standard gluon densities generated according to the collinear scheme, since the integration is made over different regions (i.e. the integral over dk_t^2 is from 0 to μ^2 in the collinear approach, whereas in the CCFM formalism the integral is over all kinematically allowed k_t^2) and the matrix elements are different. This normalization factor has to be applied to the single and double resolved cross sections, but not to the direct cross section since it is independent of the gluon density. The contribution of the direct and resolved cross sections are shown in Figure 5.2. As seen, the differences between CCFM and DGLAP are due to differences in the resolved contributions of the cross sections. Normalizing the CCFM cross section to the charm data at $\sqrt{s} = 200$ GeV

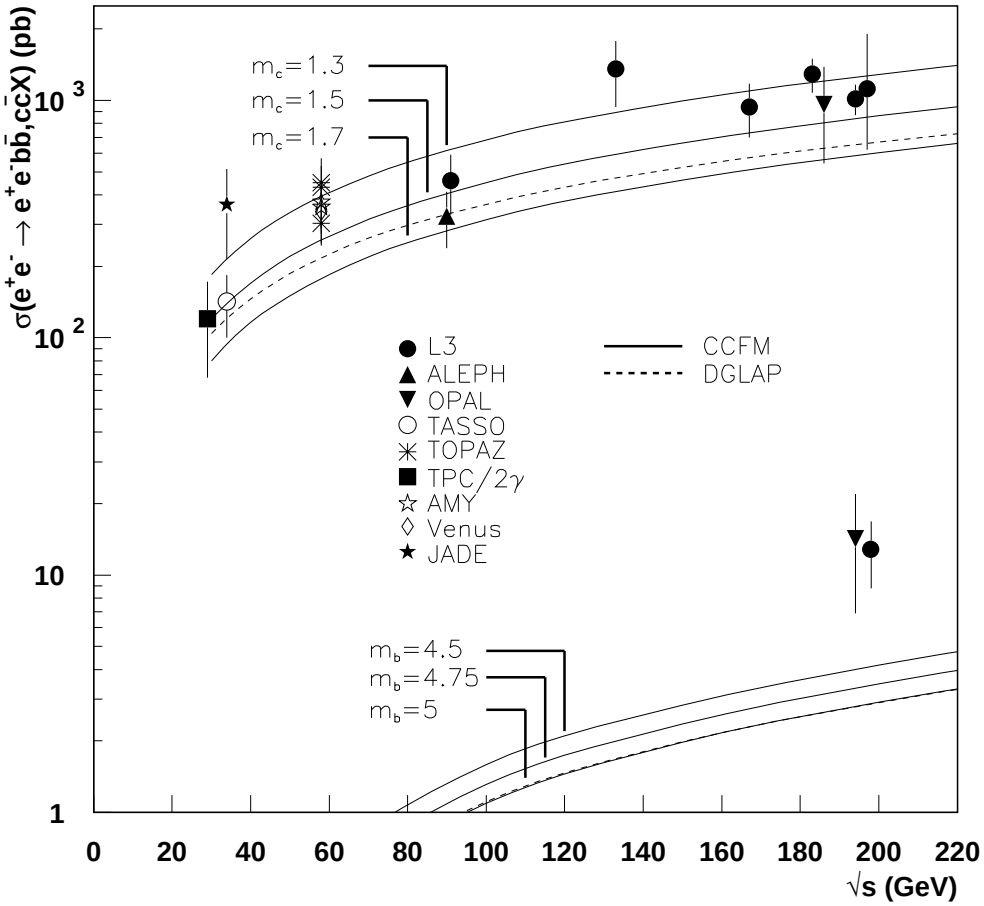

Figure 5.1: *The charm and beauty cross sections calculated with k_t-factorization compared to the DGLAP approach and data.*

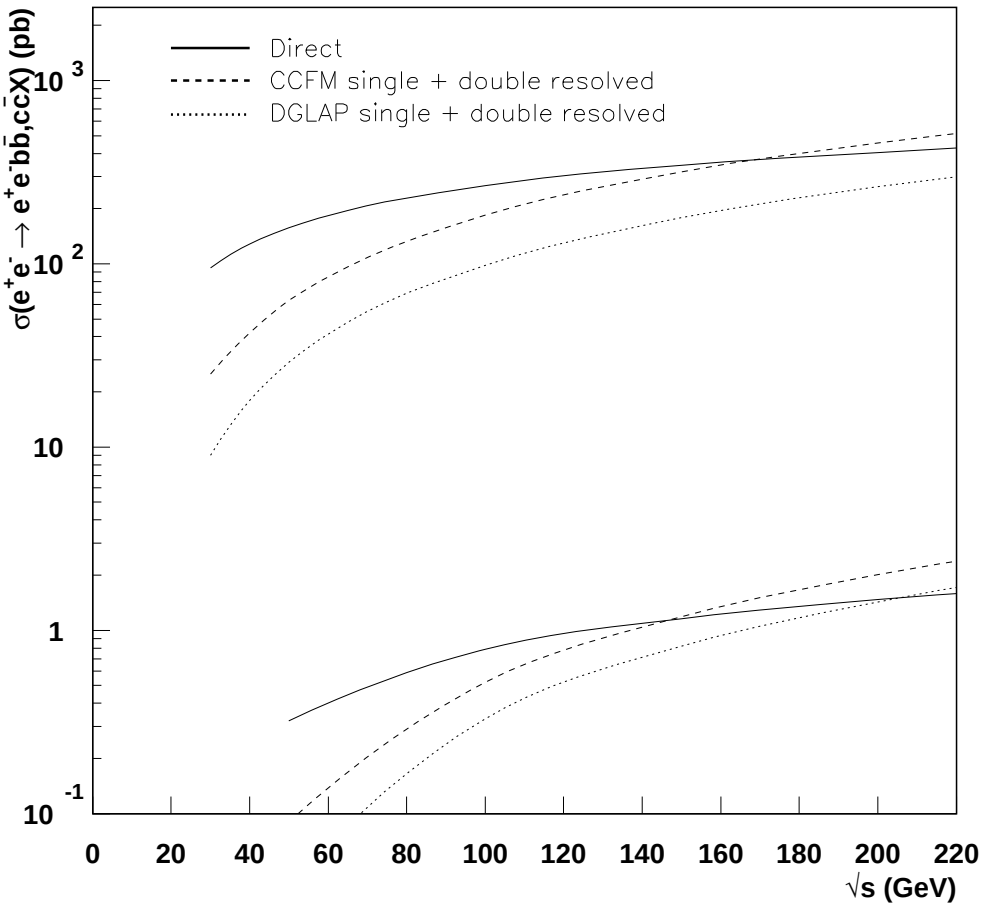

Figure 5.2: *The direct and resolved cross sections in heavy quark production calculated with CCFM and DGLAP.*

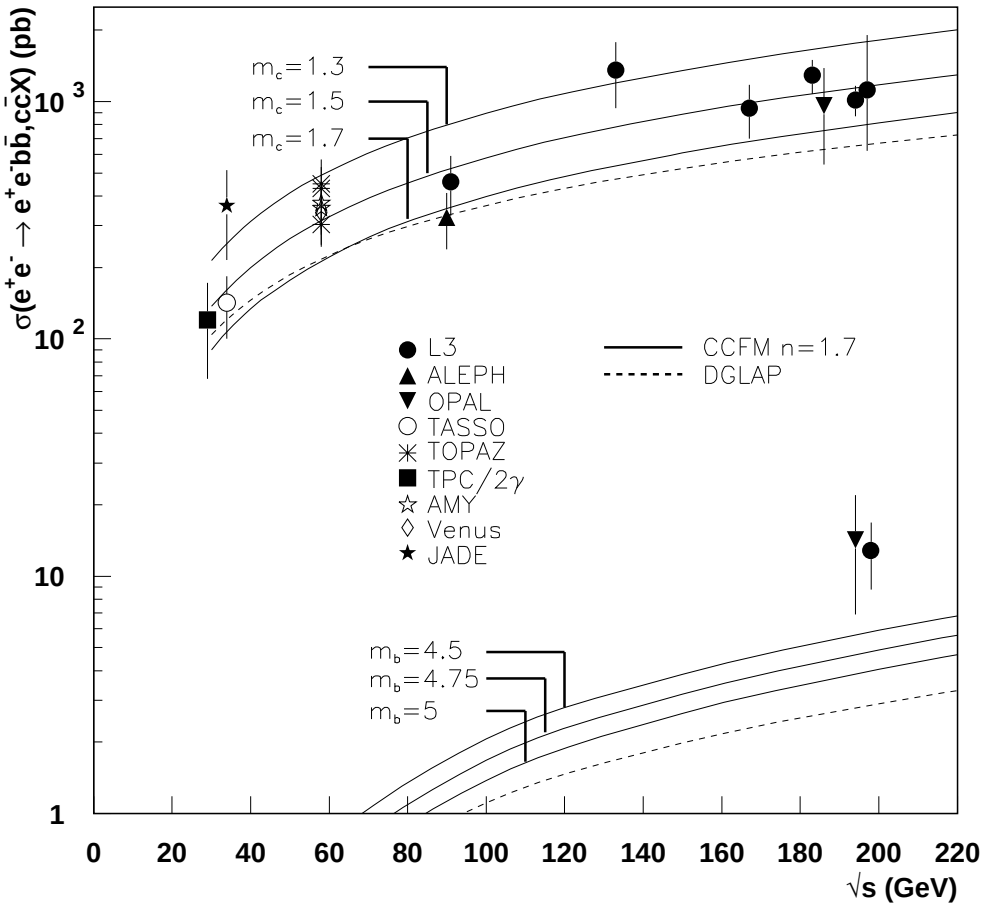

Figure 5.3: *The cross sections for heavy quark production calculated with CCFM and normalized to charm data at* $\sqrt{s} = 200$ *GeV with a factor* $n = 1.7$*, compared to DGLAP predictions and data.*

for $m_c = 1.5$ GeV, by applying a normalization factor $n = 1.7$ to the single and double resolved cross sections, gives a much steeper behaviour of the total cross section, as seen in Figure 5.3. However, the CCFM predictions are still in good agreement with the charm data at $\sqrt{s} < 200$ GeV. The normalization also improves the situation for the $b\bar{b}$ cross section, where our calculations give $\sigma_{b\bar{b}} = 4.9$ pb at $\sqrt{s} = 200$ GeV. This can be compared to standard collinear NLO predictions which give $\sigma_{b\bar{b}} \approx 4$ pb [11] and results based on [51], giving $\sigma_{b\bar{b}} = 1.9$ pb using a KMR gluon density, and $\sigma_{b\bar{b}} = 2.7$ pb using a GBW gluon density at the same energy. The CCFM cross sections are of the same order but a bit larger than NLO standard calculations, which has also been observed in ep collisions at HERA. Thus, the improvement is not sufficient fully to describe the $b\bar{b}$ data, which is still a factor 2-3 above predictions.

5.3 e^+e^- and $\gamma\gamma$ cross sections at TESLA

The CCFM predictions for heavy quark production in e^+e^- collisions at TESLA energies are shown in Figure 5.4. Here, the normalization factor $n = 1.7$ has been applied for the resolved cross sections. With a charm mass of $m_c = 1.5$ GeV the CCFM predictions at $\sqrt{s} = 500$ (800) GeV are

$$\sigma_{e^+e^- \to e^+e^- c\bar{c}X} = 2770 \text{ (4165) pb.}$$

For beauty, the predictions are

$$\sigma_{e^+e^- \to e^+e^- b\bar{b}X} = 17.06 \text{ (30.72) pb}$$

using a beauty mass of $m_b = 4.75$ GeV.

Figure 5.5 shows the charm and beauty cross sections in $\gamma\gamma$ collisions at TESLA energies calculated using the CCFM evolution. The normalization factor $n = 1.7$ has been applied to the resolved contributions. At $\sqrt{s} = 500$ (800) GeV, the predicted cross sections are

$$\sigma_{\gamma\gamma \to c\bar{c}X} = 269 \text{ (359) nb}$$

for charm and

$$\sigma_{\gamma\gamma \to b\bar{b}X} = 4.18 \text{ (6.38) nb}$$

for beauty. Also here, the masses $m_c = 1.5$ GeV and $m_b = 4.75$ GeV were used. Figure 5.5 also shows the resolved contributions of the cross sections. As seen, the single and double resolved cross sections dominate the total cross section at these energies. The reason for this is that the direct contribution, in contrast to the resolved ones, decreases with energy, and is only about 1% of the total cross section at $\sqrt{s} = 100$ GeV.

5.4 Uncertainties

The cross section for heavy quark production depends on the unintegrated gluon density and the constituent cross section, as we have discussed in Chapter 3. These in turn depend on a few parameters which are not fixed by theory but have to be determined from fits to experimental data, and therefore give rise to some uncertainties in the calculations. These uncertainties are discussed below and shown in Figure 5.6 for e^+e^- collisions.

The CCFM evolution of the unintegrated gluon density is sensitive to the input gluon density, the starting scale μ_s and the starting emission angle $\bar{q}_s$. As disussed in Chapter 4, the default values in this analysis are $\mu_s = \bar{q}_s = 1.4$ GeV, obtained from a fit to the parton distribution in the proton [47], with a GRV input distribution. The gluon densities obtained with $\mu_s = 1$ GeV and $\bar{q}_s = 1.4$ GeV, and SaS input distribution with $\mu_s = \bar{q}_s = 1.4$ GeV showed the largest differences compared to the gluon density obtained

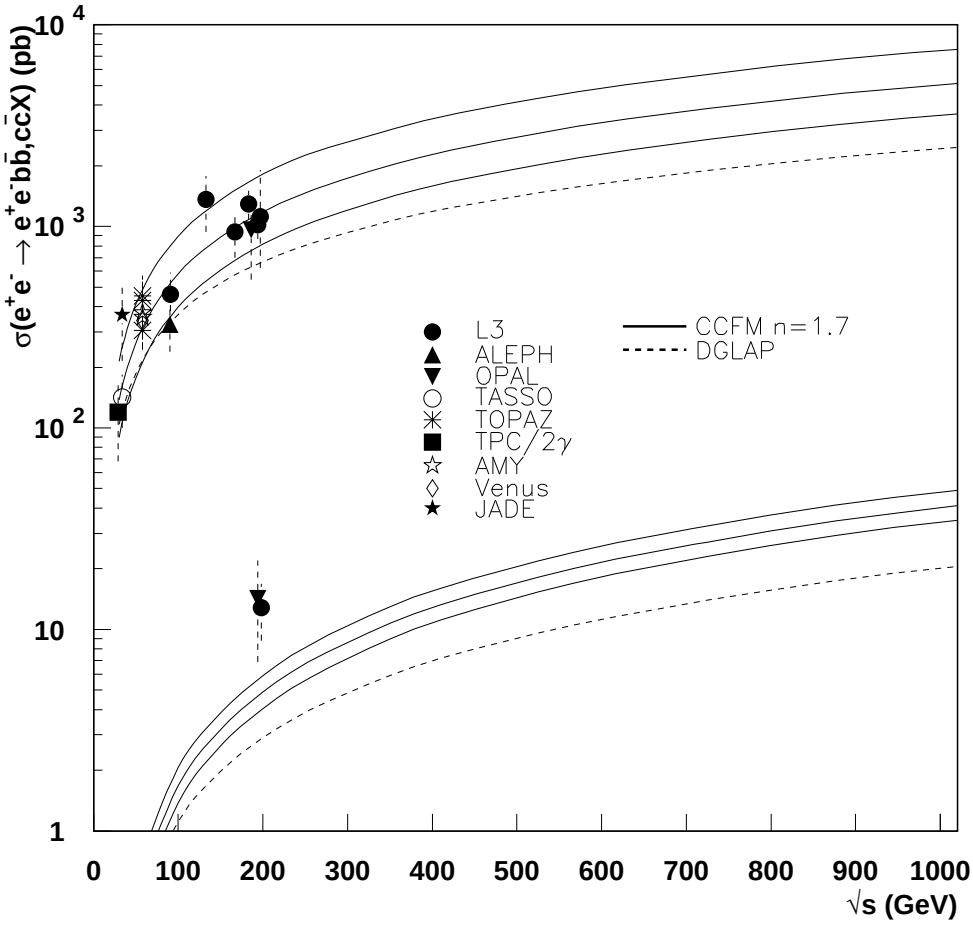

Figure 5.4: *Heavy quark cross section predictions for e^+e^- collisions at TESLA energies calculated with CCFM and compared to the DGLAP predictions. For CCFM, the quark masses $m_c = 1.3, 1.5, 1.7$ GeV and $m_b = 4.5, 4.75, 5$ GeV were used, where the smallest mass gives the largest cross section. For DGLAP, $m_c = 1.5$ GeV and $m_b = 4.75$ GeV. Also, the normalization factor $n = 1.7$ was applied to the resolved cross sections in the CCFM calculations.*

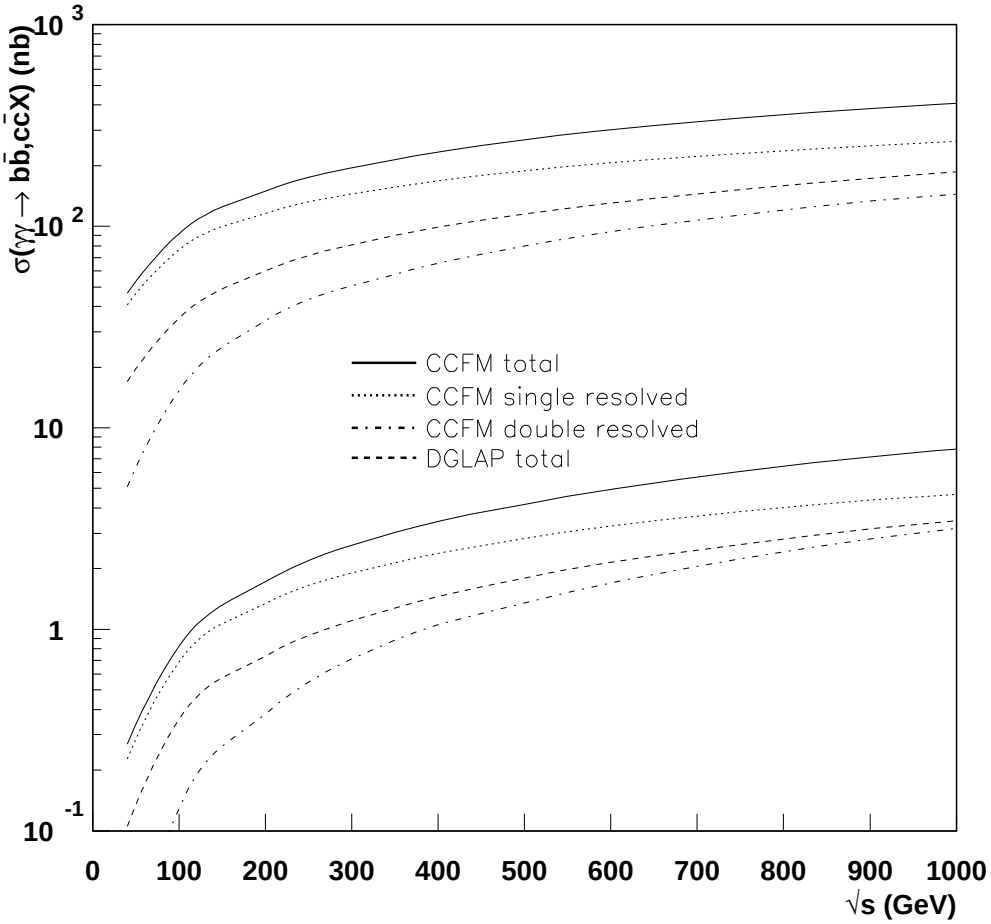

Figure 5.5: *Heavy quark cross section predictions for $\gamma\gamma$ collisions at TESLA energies. The masses $m_c = 1.5\ GeV$ and $m_b = 4.75\ GeV$ were used.*

with the default option (see Figure 4.7). Therefore, the cross sections were calculated also with these gluon densities to get an estimate of the error.

The strong coupling constant α_s is, despite its name, not a constant, but varies with the energy scale μ, according to (in a first approximation)

$$\alpha_s = \frac{12\pi}{(33 - 2 \cdot n_f) \ln(\frac{\mu^2}{\Lambda^2})}. \tag{5.2}$$

Here, n_f is the number of quark flavours with mass less than the energy scale μ, and Λ is a constant which has to be determined by experiments. The value of Λ also depends on the order that the process is calculated at. However, it is not clear how to compare the value of Λ used in the CCFM approach with the one used in NLO DGLAP, since the first order in the CCFM approach includes some second order diagrams in the DGLAP approach. The default value was chosen to be $\Lambda = 0.2$ GeV, which was also used in the evolution of the unintegrated gluon density, but $\Lambda = 0.34$ GeV (used in [28]) was also tested.

The energy scale μ is of the order of the typical momentum transfer, but the exact choice of scale should be such that the higher order contributions in the perturbative expansion of the cross section are minimal. The standard choice is $\mu^2 = m^2 + p_t^2$, where m is the heavy quark mass and p_t is the transverse momentum of the heavy quarks in the center of mass frame of the heavy quark system. To show the effect of the choice of μ, the scale $\mu^2 = 4m^2$ is also used here as a comparison.

The quark masses. Since the quarks are always confined in colorless hadrons, their masses cannot be measured directly. Instead, the masses must be extracted from hadron properties. However, this can be done in various ways depending on the exact definition of the quark masses, and different methods lead to slightly different results. Therefore, the heavy quark masses are varied such that 4.5 GeV $< m_b <$ 5 GeV and 1.3 GeV $< m_c <$ 1.7 GeV. This variation of the quark masses gives the largest uncertainty, and can therefore be used as an estimate of the total uncertainty, as seen in Figure 5.4, for example.

In Figure 5.6 is shown the cross sections for heavy quark production in e^+e^- collisions, calculated with different choices of Λ, μ^2 and unintegrated gluon densities. One can see that a change in Λ from $\Lambda = 0.2$ GeV to $\Lambda = 0.34$ GeV gives the largest variation of the cross sections, while changing μ^2 and the gluon density only makes smaller variations. However, all these uncertainties are small compared to a change in the quark masses, see Figure 5.1.

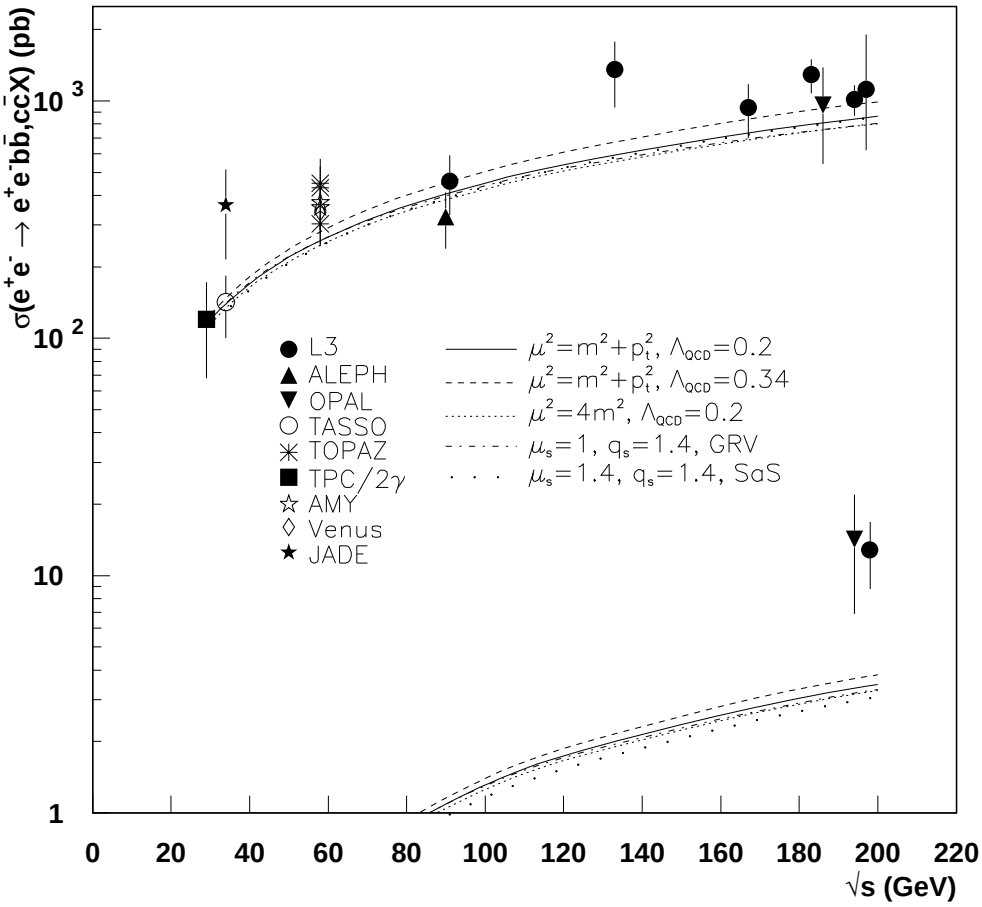

Figure 5.6: *The cross section dependence on Λ, μ^2 and different unintegrated gluon densities.*

Chapter 6

Conclusions

The unintegrated gluon density for the photon was obtained with the full CCFM evolution for the first time. The CCFM evolved gluon density for the photon was used as input in the MC generator CASCADE, and cross sections for heavy quark production in e^+e^- collisions were calculated and compared to LEP data. Also, predictions for charm and beauty production in e^+e^- and $\gamma\gamma$ collisions at TESLA energies are given.

In e^+e^- collisions, the obtained cross sections were somewhat larger than NLO DGLAP predictions, but in good agreement with the charm data from LEP. The CCFM approach made a slight improvement compared to the standard collinear approach for the beauty cross sections. However, the improvement did not fully account for the discrepancy to the $b\bar{b}$ data.

The next step of this analysis would be to calculate heavy quark cross sections in ep collisions and compare to HERA data. This was not possible within the framework of this thesis, since the analysis would be based on jet reconstruction, and the parton showering is not yet included in CASCADE.

Chapter 7

Acknowledgements

I would like to thank Leif Jönsson and Hannes Jung for supervision and help with everything. For some reason, I would also like to thank Albert Knutsson and Martin Karlsson. Also, thanks to all the people at the Department of High Energy Physics. This work was supported by INTAS grant 00-00679.

Bibliography

[1] B. Badelek *et al.* [ECFA/DESY Photon Collider Working Group Collaboration], "TESLA Technical Design Report, Part VI, Chapter 1: Photon collider at TESLA," arXiv:hep-ex/0108012

[2] M. M. Muhlleitner, M. Kramer, M. Spira and P. M. Zerwas, *Phys. Lett.* **B 508** (2001) 311

[3] I. F. Ginzburg and M. V. Vychugin, arXiv:hep-ph/0201117

[4] T. Behnke, S. Bertolucci, R. D. Heuer and R. Settles, "TESLA: The superconducting electron positron linear collider with an integrated X-ray laser laboratory. Technical design report. Pt. 4: A detector for TESLA," DESY-01-011

[5] D. Buskulic *et al.* (ALEPH Collaboration), *Phys. Lett.* **B 355** (1995) 595

[6] M. Acciarri *et al.* (L3 Collaboration), *Phys. Lett.* **B 453** (1999) 83

[7] M. Acciarri *et al.* (L3 Collaboration), *Phys. Lett.* **B 467** (1999) 137

[8] M. Acciarri *et al.* (L3 Collaboration), *Phys. Lett.* **B 503** (2001) 10

[9] M. Acciarri *et al.* (L3 Collaboration), *Phys. Lett.* **B 514** (2001) 19

[10] M. Acciarri *et al.* (L3 Collaboration), *Phys. Lett.* **B 536** (2002) 217

[11] The L3 Collaboration, L3 Note 2761

[12] The OPAL Collaboration, OPAL Physics Note PN455

[13] G. Abbiendi *et al.* (OPAL Collaboration), *Eur. Phys. J.* **C 16** (2000) 579

[14] G. Altarelli, T. Sjöstrand and F. Zwirner, Physics at LEP2, CERN 96-01 (1996)

[15] C. Adloff *et al.* (H1 Collaboration), *Nucl. Phys.* **B 545** (1999) 21

[16] C. Adloff *et al.* (H1 Collaboration), *Phys. Lett.* **B 467** (1999) 156; erratum ibid.

[17] C. Adloff *et al.* (H1 Collaboration), *Phys. Lett.* **B 518** (2001) 331

[18] J. Breitweg *et al.* (ZEUS Collaboration), *Eur. Phys. J.* **C 6** (1999) 67

[19] J. Breitweg *et al.* (ZEUS Collaboration), *Eur. Phys. J.* **C 12** (2000) 35

[20] J. Breitweg *et al.* (ZEUS Collaboration), *Eur. Phys. J.* **C 18** (2001) 625

[21] F. Abe *et al.* (CDF Collaboration), *Phys. Rev. Lett.* **71** (1993) 500

[22] F. Abe *et al.* (CDF Collaboration), *Phys. Rev. Lett.* **71** (1993) 2396

[23] F. Abe *et al.* (CDF Collaboration), *Phys. Rev. Lett.* **75** (1995) 1451

[24] B. Abbot *et al.* (D0 Collaboration), *Phys. Lett.* **B 487** (2000) 264

[25] H. Jung, Unintegrated parton densities applied to heavy quark production in the CCFM approach, in *Procedings of the Rinberg workshop on 'New trends in HERA physics', Rinberg Castle, Tegernsee, Germany* (2001), hep-ph/0109146

[26] H. Jung, Heavy quark production at the TEVATRON and HERA using k_t-factorization with CCFM evolution, Lund University, 2001, hep-ph/0110034, DESY 01-136

[27] M. Glück, E. Reya and A. Vogt, *Z. Phys* **C 67** (1995) 433

[28] M. Drees *et al.*, *Phys. Lett.* **B 306** (1993) 371

[29] V. Gribov and L. Lipatov, *Sov. J. Nucl. Phys.* **15** (1972) 438 and 675

[30] L. Lipatov, *Sov. J. Nucl. Phys.* **20** (1975) 94

[31] G. Altarelli and G. Parisi, *Nucl. Phys.* **B 126** (1977) 298

[32] Y. Dokshitzer, *Sov. Phys. JETP* **46** (1977) 641

[33] E. Kuraev, L. Lipatov and V. Fadin, *Sov. Phys. JETP* **44** (1976) 443

[34] E. Kuraev, L. Lipatov and V. Fadin, *Sov. Phys. JETP* **45** (1977) 199

[35] Y. Balinsky and L. Lipatov, *Sov. J. Nucl. Phys.* **28** (1978) 822

[36] M. Ciafaloni, *Nucl. Phys.* **B 296** (1988) 49

[37] S. Catani, F. Fiorani and G. Marchesini, *Phys. Lett.* **B 234** (1990) 339

[38] S. Catani, F. Fiorani and G. Marchesini, *Nucl. Phys.* **B 336** (1990) 18

[39] G. Marchesini, *Nucl. Phys.* **B 445** (1995) 49

[40] H. Jung, *Comp. Phys. Comm.* **143** (2002) 100

[41] T. Sjöstrand, *Comp. Phys. Comm.* **82** (1994) 74

[42] H. Plothow-Besch, 'The Parton Distribution Function Library',
Int. J. Mod. Phys. **A 10** (1995) 2901

[43] The CERN Program Library

[44] W. H. Press *et al.*, *Numerical recepies in Fortran, second edition* (Cambridge University Press, New York, 1992)

[45] M. Glück, E. Reya and A. Vogt, *Phys. Rev.* **D 45** (1992) 3986

[46] G. Ingelman, A. Edin and J. Rathsman, *Comp. Phys. Comm.* **101** (1997) 108

[47] H. Jung and G. P. Salam, *Eur. Phys. J.* **C 19** (2001) 351

[48] S. P. Baranov *et al.*, *Eur. Phys. J.* **C 24** (2002) 425

[49] G. A. Schuler and T. Sjöstrand, *Phys. Lett.* **B 276** (1996) 193

[50] S. Catani, M. Ciafaloni and F. Hautmann, *Nucl. Phys.* **B 366** (1991) 135

[51] L. Motyka and N. Timneanu, arXiv:hep-ph/0209029